Lab on a Chip

CRITICAL REVIEW

View Article Online
View Journal | View Issue

Check for updates

Cite this: *Lab Chip*, 2021, **21**, 2069

Received 23rd February 2021,
Accepted 11th May 2021

DOI: 10.1039/d1lc00144b

rsc.li/loc

Microfluidic formation of crystal-like structures

Francesco Del Giudice, *[a] Gaetano D'Avino [b] and Pier Luca Maffettone [b]

Crystal-like structures find application in several fields ranging from biomedical engineering to material science. For instance, droplet crystals are critical for high throughput assays and material synthesis, while particle crystals are important for particles and cell encapsulation, Drop-seq technologies, and single-cell analysis. Formation of crystal-like structures relies entirely on the possibility of manipulating with great accuracy the micrometer-size objects forming the crystal. In this context, microfluidic devices offer versatile tools for the precise manipulation of droplets and particles, thus enabling fabrication of crystal-like structures that form due to hydrodynamic interactions among droplets or particles. In this review, we aim at providing an holistic representation of crystal-like structure formation mediated by hydrodynamic interactions in microfluidic devices. We also discuss the physical origin of these hydrodynamic interactions and their relation to parameters such as device geometry, fluid properties, and flow conditions.

1 Introduction

Crystals are defined as homogeneous pieces of solid substance having a natural geometrical regular form with symmetrically arranged planes.[1] The term crystal has seen a substantial evolution over time, and nowadays it refers to systems, either liquid or solid, that display a certain degree of regularity or order. In this context, microfluidics emerged as a very suitable field to enable the formation and the study of crystal-like structures owing to the possibility of controlling fluid and solid elements at the sub-micrometer scale.

Crystal-like structures in microfluidic devices, hereafter microfluidic crystals, can either be formed thanks to external fields (*e.g.*, electric or magnetic field) or because of hydrodynamic interactions among the different objects forming the crystal. In order to experience hydrodynamic interactions, the objects need to 'feel' each other, meaning

Francesco Del Giudice

Francesco Del Giudice is a Senior Lecturer and a Chartered Chemical Engineer at Swansea University (UK). Francesco obtained BEng, MSc and PhD in Chemical Engineering at University of Naples Federico II. During the PhD period, Francesco was a visiting researcher at Glasgow University. Francesco then moved to Okinawa, Japan, for a Postdoctoral Scholarship at Okinawa Institute of Science and Technology Graduate School. After joining Swansea University, Francesco first secured an EPSRC New Investigator Award grant and then established the Rheological Microfluidic lab. Francesco is currently engaged in research activities at the boundary between chemical and biomedical engineering.

Gaetano D'Avino

Gaetano D'Avino is Associate Professor at the Department of Chemical Engineering, Materials and Industrial Production of the University of Naples Federico II. He received his degree cum laude in Chemical Engineering from University of Naples Federico II on 2004. In 2007, he got his PhD at the Department of Chemical Engineering of University of Naples Federico II. His research activity is mainly focused on the simulations of particle dynamics in complex systems, prediction of rheological properties of suspensions, and development of efficient numerical methods for simulating the fluid dynamics of complex materials.

---

[a] *System and Process Engineering Centre, College of Engineering, Fabian Way, Swansea, SA1 8EN, UK. E-mail: francesco.delgiudice@swansea.ac.uk; Tel: +44 (0)1792 604027*
[b] *Dipartimento di Ingegneria Chimica, dei Materiali e della Produzione Industriale, Universitá degli Studi di Napoli Federico II, Piazzale Tecchio 80, 80125 Naples, Italy*

that the local concentration should be sufficiently large to enable hydrodynamic interactions to take place. In such conditions, hydrodynamic interactions can promote the self-assembly of individual objects in crystal-like structures depending on several parameters such as channel geometry, fluid properties, and flow rate.

Microfluidic crystals, especially droplet and particle crystals, are not only important from a fundamental point of view, as they are found in a variety of microfluidic applications including digital PCR, synthesis of colloidal structures and single-cell analysis. So far, however, droplet and particle crystals have never been presented under a unified framework, which is helpful in understanding the self-assembly phenomena mediated by hydrodynamic interactions with the ultimate goal of generating new optimised technologies.

In this review, we aim at providing a holistic view of microfluidic crystals formed as results of droplet and particle self-assembly promoted by hydrodynamic interactions (Fig. 1). We believe that a multidisciplinary approach to microfluidic manipulation of crystals could open up the way to new microfluidic applications. We will mainly focus on microfluidic crystals and their applications, while referring the reader to other recent reviews to receive a broader overview about the advancements of each specific application.

The review is organized as follows. In section 2, we will first present the relevant dimensionless numbers required to understand the effect of the parameters governing the self-assembly dynamics. In section 3, we will discuss the formation of droplet crystals covering fundamental and application aspects. Similarly, in section 4, we will focus on self-assembly of particle crystals. In section 5, we will discuss recent applications in compartmentalisation involving both droplet and particle crystals. Finally, we will draw some conclusions and suggest future directions.

Pier Luca Maffettone

Pier Luca Maffettone, PhD, is Full Professor in Chemical Engineering at University of Naples "Federico II". He graduated in 1988 in Chemical Engineering and received the Ph.D. in Chemical Engineering at the University of Naples Federico II in 1993. His main research activity is focused on modeling and simulation of the flow behavior of soft matter as suspensions, liquid crystals, polymer blends and emulsions. Recent activities are related to microfluidics and lab-on-chip applications with complex liquids. He acted as Member of the Executive Committee of the European Society of Rheology (2014–20) and has been nominated fellow of the Society of Rheology (class 2018).

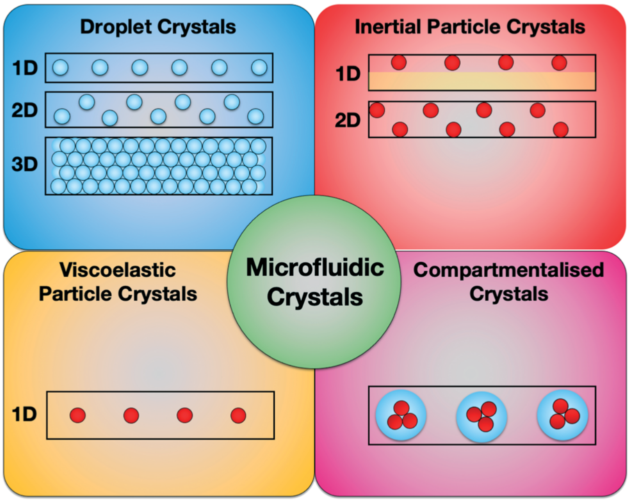

Fig. 1 Summary of the microfluidic crystal types reviewed here.

2 Dimensionless numbers

In this section, we introduce some dimensionless numbers helpful to understand the effect of the relevant parameters on the self-assembly dynamics and commonly used in many of the reviewed works. In general, dimensionless numbers are very useful to compare the relevant forces operating in a system, as well as to offer an easy way to compare experiments and simulations carried out at different operating conditions. We will follow the definitions reported in the review by Squires and Quake.[2]

The importance of inertial and viscous forces during flow can be quantified by the Reynolds number defined as:

$$\mathrm{Re} = \frac{\text{Inertial Forces}}{\text{Viscous Forces}} = \frac{\rho u L_c}{\eta}, \qquad (1)$$

where ρ is the fluid density, u is a characteristic fluid velocity (usually taken as the average fluid velocity), L_c is a characteristic length scale of the flow (*e.g.*, for cylindrical channels, it corresponds to the tube diameter D), and η is the fluid viscosity. When the Reynolds number is much larger than one, inertial forces overcome viscous forces, and *vice versa*.

When the fluid presents a certain amount of elasticity, for instance as in the case of aqueous solutions with the addition of polymers, the dimensionless number employed to characterise the strength of the elastic forces is the Deborah number defined as:

$$\mathrm{De} = \frac{\text{Characteristic time of the fluid}}{\text{Characteristic time of the flow}} = \frac{\lambda}{t_f}, \qquad (2)$$

where λ is the characteristic time of the fluid (*e.g.*, the longest relaxation time) and t_f is the flow characteristic time. For instance, in a circular pipe, the flow characteristic time can be expressed as $t_f = D/u$. Another way to characterise the fluid elasticity is *via* the Weissenberg number defined as the ratio between the first normal stress difference and the shear stress. In the linear regime (*i.e.*, for small deformations of the liquid, meaning small flow rate values in microchannels) this can be expressed as λ divided by a flow deformation time (*e.g.*, the inverse of a characteristic shear rate), analogously to the Deborah number. In this review, we use the Deborah number because most of the works on microfluidic crystals featuring viscoelastic fluids employed this dimensionless number.

The ratio between inertial and viscoelastic forces is quantified by the elasticity number defined as:

$$\mathrm{El} = \frac{\text{Elastic Forces}}{\text{Inertial Forces}} = \frac{\mathrm{De}}{\mathrm{Re}}. \tag{3}$$

In a multiphase system made of two non-miscible liquids interfacial properties play a relevant role. The ratio between viscous forces and interfacial forces is quantified using the capillary number:

$$\mathrm{Ca} = \frac{\text{Viscous Forces}}{\text{Interfacial Forces}} = \frac{\eta u}{\gamma}, \tag{4}$$

where γ is the interfacial tension between the two liquids. The values of η and u can either be those of the droplet material (dispersed phase) or of the material surrounding the droplet (continuous phase).[3]

We also introduce the particle Reynolds number that is widely employed in the discussion of particle crystals formed during inertial flow (section 4):

$$\mathrm{Re}_\mathrm{p} = \frac{\rho u d_\mathrm{p}}{\eta} = \mathrm{Re}\beta, \tag{5}$$

where d_p is the diameter of the flowing particle and β is the confinement ratio defined as:

$$\beta = \frac{d_\mathrm{p}}{L_\mathrm{c}}. \tag{6}$$

3 Droplet crystals

Before reviewing the literature on droplet crystals, it is worth to introduce here few concepts regarding droplet formation. Droplets are generally formed when two non-miscible liquids 'meet' at a microfluidic junction: the competition between capillary forces and viscous forces at the interface between the two liquids results in the formation of droplets having different sizes.[2] The fluid that surrounds the droplet is referred to as the continuous phase, while the fluid forming the droplet is the dispersed phase. It has been shown that droplets can form in microfluidic devices having, among others, three geometries: coaxial, flow focusing, and T-junction.[3] The size of the droplets as well as the droplet regime investigated (*e.g.*, dripping or jetting regime) strongly depend upon the microfluidic geometry, the fluid properties, and the flow conditions.[3] A detailed description of the droplet formation mechanism falls outside the scope of this review; we refer the interested reader to the review by Nunes *et al.*[3] or the more recent ones by Zhu *et al.*[4] and Guerrero *et al.*[5]

3.1 Formation and stability of droplet crystals: hydrodynamic interactions among droplets

In this section, we review the literature related to the effect of hydrodynamic interactions among droplets on the overall stability of the droplet crystal. This is especially important to control the formation of droplet crystals used for analytical chemistry applications as well as for the fabrication of colloidal structures (see section 3.3 for more details). We will focus on the available techniques and the experimental results on droplet crystal self-assembly, without going into the details of the mathematical model involved in the descriptions of the hydrodynamic potentials and the flow fields. The interested reader may refer to the two reviews[6,7] by Beatus, Bar-ziv and Tlusty, where the full details regarding the physical equations describing interactions among droplets are reported and discussed.

The first observation of droplet generation in a microfluidic device together with the first evidence of crystal-like structures formation was presented by Thorsen *et al.*[11] A T-junction with width w = 30 μm and height h = 9 μm followed by an expansion region having the same height but width w = 60 μm was used to generate water in oil droplets. The droplets were formed at a frequency of 20–80 hertz and, depending on the average imposed pressure between oil and water, they observed a variety of crystal-like structures in the expansion region. In particular, they observed 1D crystals made by equally spaced droplets, 1D crystals formed by necklace of droplets attached to each other, and 2D crystals made of adjacent droplets forming a crystal along the expansion width. Despite the work of Thorsen *et al.*[11] was the first to show the formation of droplet crystals, the main outcome of their work was the formation of uniformly distributed droplets (a significant improvement over macroscopic techniques); they did not investigate the stability of the crystals, nor clarified the origin behind the formation of such crystals. In several microfluidic applications such as digital polymerase chain reaction PCR, particle/cell encapsulation and synthesis of particles, the relation among external flow parameters, hydrodynamic interactions, and resulting crystal is very important to establish a general framework to create *ad hoc* crystal-like structures that target specific applications (see section 3.3 for a more detailed discussion). Beatus *et al.*[8] were the first to study the stability of 1D droplet crystals as a function of the hydrodynamic interactions between adjacent droplets (Fig. 2a). Similarly to Thorsen *et al.*,[11] they formed water in oil droplets using a T-junction having a height of h = 10 μm and a width of w = 35 μm, followed by an expansion with the same height and a width of w = 250 μm (when the width of the channel is significantly larger than its height, the device is also referred as 'Hele-Shaw' cell,[12] because the flow can be approximated as a Poiseuille-like flow along the height h and as a potential flow along the width w). The diameter of the droplet formed at the T-junction was larger than the height of the microfluidic device: therefore, as the droplets approached the

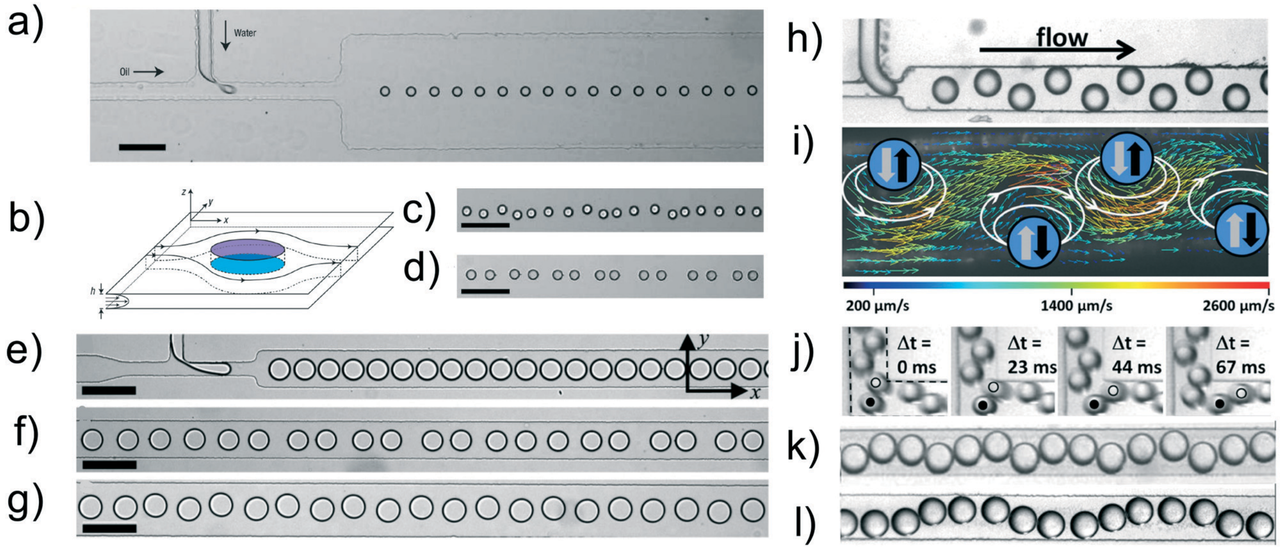

Fig. 2 a) 1D microfluidic crystal made of water droplets (dispersed phase) surrounded by oil (continuous phase). The height of the channel is h = 10 μm. The width at the T-junction is w = 35 μm, while that along the expansion area is 250 μm. Scale bar is 100 μm b) schematic of a droplet in a 'pancake' configuration as a result of the confinement along the z-direction. The continuous phase flows along the x-direction. The velocity profile is parabolic along the z-direction and a potential flow in the xy-plane. c) Image of transversal acoustic waves. d) Image of longitudinal acoustic waves. Panels a)–d) are reprinted by permission from Springer Nature: *Nature Physics*, Beatus *et al.*,[8] Phonons in a one-dimensional microfluidic crystal, Copyright Springer Nature, 2006. e) Droplets of water in oil subjected to strong lateral confinement. f) Confined droplets exhibit longitudinal wave motion. g) Confined droplets exhibit transversal wave motion. Panels e)–g) are reprinted with permission from Beatus *et al.*,[9] *Physical Review Letter*, **99**, 124502, Copyright 2007 by the American Physical Society. h) Generation of microfluidic crystals using a step-emulsification geometry. i) Flow field determined by particle image velocimetry in the lab frame. The relevant dipolar flow fields around each droplet in the co-moving frame of the droplets are sketched by white arrows. The second half of the dipolar flow field close to the channel wall is omitted for the sake of clarity. The transverse forces resulting from the dipolar flow fields from leading and trailing droplets are shown as grey and black arrows, respectively. j) Microscopy time series showing the droplet reorganization at a 90° bend. The boundaries of the bend were indicated in the first image. The droplet marked with a dot is repelled from the corner due to its hydrodynamic image and the trailing droplet marked with a circle is squeezed between the leading droplet and the wall and propelled longitudinally out of the corner. k and l) Travelling sine waves with different wavelength as generated by periodic defects for two different droplet sizes. The width of all microfluidic channels is w = 210 μm. Panels h)–l) are reprinted from Fleury *et al.*,[10] Mode coupling of phonons in a dense one-dimensional microfluidic crystal, *New Journal of Physics*, **16**, 063029, 2014, https://doi.org/10.1088/1367-2630/16/6/063029.

expansion area, the droplet assumed a 'pancake' configuration, *i.e.*, more squeezed along the height than the width (Fig. 2b). The 1D crystal observed by Beatus *et al.*[8] was stable only near the beginning of the expansion area, while displaying both transversal and longitudinal oscillations further downstream (Fig. 2c and d). These acoustic waves reminded the authors of the acoustic 'phonons' observed in solid-state physics. The origin of these waves were ascribed to the hydrodynamic interactions between consecutive droplets. In particular, for droplets confined along one direction, as in the case of pancake-like droplets, they observed a strong mismatch between the velocity of the droplets and that of the continuous phase. This was due to the drag experienced by the droplets because of their confinement between the floor and the ceiling of the microfluidic device: in these conditions, the droplets disturbed the flow of the continuous phase, resulting in the formation of a dipole-like flow field around the droplet (Fig. 2b). The hydrodynamic interactions between subsequent droplets were the result of superposition of flow dipoles that generated a long-range propagation of a wave that disrupted the stability of the crystal. The same authors also observed that the flow-disturbance around the droplets propagated longitudinally over the expansion area causing the destruction of the 1D crystal formed at the T-junction. Similar results were obtained by Liu *et al.*[13] that performed numerical simulations aimed at studying the stability of a system of confined droplets. They concluded that the instability in the droplet configuration was due to two factors: i) the non-linearity in the hydrodynamic potential and ii) interactions between longitudinal and transversal waves. The analytical expression for the interaction forces between two closely spaced droplets has been obtained by Sarig *et al.*[14] with a follow up analysis carried out by Green.[15] From an application point of view, the results presented above are extremely important because they provide some arguments on how to design the microfluidic device for targeted applications. For instance, for the fabrication of crystals made of pancake-like structure using UV (see the recent review by Wang and Wang[16]), it is important to design the expansion channel short enough so that the photo-polymerisation takes place before any longitudinal or transversal instability begins. For applications such as digital PCR,[17] it is important to fill in the expansion area of the microfluidic device with as many droplets as possible: if both transversal and longitudinal waves take place simultaneously, they may result in a chaotic behaviour[8] that leads to the destruction of the crystal, thus making the whole process of filling in the expansion area with droplets unpredictable and not optimised, with negative implications on the throughput of a digital-PCR assay.

In their pioneering work, Beatus *et al.*[8] mainly focused on pancake droplets that were practically unconfined along the channel width in the expansion. In a follow-up study,[9] the same authors analysed the effect of the confinement on the stability of the 1D crystal-like structures (Fig. 2e–g). The 1D crystal-like structures were formed by water in oil droplets flowing in a microfluidic channel with constant height of h = 10 μm and different values of the expansion width to simulate the transition from unconfined (w = 250 μm) to confined (w = 50 μm) conditions. They observed that the 1D crystal was more stable compared to the one reported in the previous work[8] because the interactions that caused the vibrational modes along the channel width were screened exponentially by the lateral walls. Under a physical point of view, an increase in the confinement resulted in a symmetry breaking between longitudinal and transversal vibration modes, with the transversal modes being stronger in magnitude than the longitudinal ones. The screening of the long-range interactions also resulted in the strengthening of the hydrodynamic interactions between consecutive droplets due to the crystal incompressibility in plug-flow configuration, *i.e.*, when the channel was nearly blocked by the droplets.

Stable production of droplet crystals is the foundation for a vast range of optimised microfluidic applications. For this reason, it is important to know in which flow conditions droplet crystals are stable and what would be the effect of flow perturbations (*i.e.*, channel defects, geometrical changes, *etc.*) on the stability of the crystal. This aspect has been considered by Fleury *et al.*,[10] who employed a step emulsification geometry[18] to produce a stable 2D zig-zag crystal made of water droplets with radius $R \approx 64$ μm in *n*-hexadecane (Fig. 2h). When the droplets entered the expansion area with height of h = 120 μm and width of w = 210 μm, they were squeezed between the floor and the ceiling of the channel, with a velocity lower than the continuous phase velocity, thus generating a flow dipole similarly to Beatus *et al.*[8] When a new droplet entered the expansion area, the hydrodynamic interactions between the flow dipole of the entering droplet and that of the leading droplet resulted into the formation of a stable zig-zag 2D crystal (Fig. 2i). Such crystal was found to be very stable along the expansion area. The introduction of a 90° bend following the expansion area (Fig. 2j), however, resulted in the droplets to become closer, and it also promoted sinusoidal waves along the full width of the microfluidic channel (Fig. 2k and l). Even though it is not possible to clearly appreciate the actual sinusoidal motion from the experimental snapshots, we invite the interested reader to access the ESI video provided by the authors.[10] In a different work,[19] the authors also performed additional experiments and numerical simulations that demonstrated the possibility of using defect patterns to excite transversal or longitudinal vibrations starting from an initial zig-zag 2D crystal. From a practical point of view, the results presented above suggest that the stability of a crystal should not be taken for granted as flow perturbations can modify the overall stability of the crystal. For instance, imperfections in the microchannel fabrication can lead to local flow modifications that propagate along the crystal with a destabilising effect (see also Thutupalli *et al.*[20] for more details).

Once the crystal has been formed within the microfluidic device, it is worth to ask whether it is stable when subjected to an applied flow. Gai *et al.*[21] studied the overall motion of a 2D droplet crystal in a microfluidic 'tapered' channel with a 5° angle leading to a constriction of 30 μm. When the crystal approached the constriction, a spatial periodicity of the droplet rearrangement was observed that could be described by the Read–Shockley model[22] for low-angle grain boundaries. They also observed that the geometry of the tapered channel, and especially the taper angle, was very important to preserve the periodicity of the spatial rearrangement in the crystal. If the taper angle was too large, a chaotic behaviour of the crystal rearrangement appeared.

The volumetric flow rate had also an effect on the dynamic of rearrangement of the microfluidic crystal.[23] At sufficiently large flow rate values, which are often essential in microfluidic high-throughput applications, the overall crystal dynamics moved from liquid-like to solid-like, and this resulted in a non-localised spatial distribution, where the local order was lost.

3.2 Formation of droplet crystals in microfluidic flows: from 1D to 3D crystals

The formation of droplet crystals in microfluidic devices strongly depends on the geometry of the microfluidic device as well as on the ratio between the flow rate of the continuous phase Q_c and the dispersed phase Q_d, as well as the capillary number Ca. Jose and Cubaud[24] employed a microfluidic device with constant height h = 250 μm having a square-shaped flow focusing droplet formation area followed by a diverging/converging channel (expansion chamber) with an angle of 45° and maximum width $w = 20\ h = 5000$ μm. Depending on the capillary number Ca and the ratio $Q_c/(Q_c + Q_d)$ at the flow focusing area, spherical droplets with diameter $h < d_0 < 2\ h$ and uniform size distribution were formed. These droplets first travelled along a square-shaped 5 mm long microchannel and then entered the diverging/converging geometry, where 1D-crystals and 2D-crystal formation was observed (Fig. 3a). The dynamic of formation of the 2D-crystals arranged in a multi-layered structure was similar to the one described in previous works.[8,10] The authors tracked a series of droplets entering the diverging/converging area (Fig. 3b) and observed that such droplets where deflected from their centreline positions because of the hydrodynamic interactions with the droplets already in

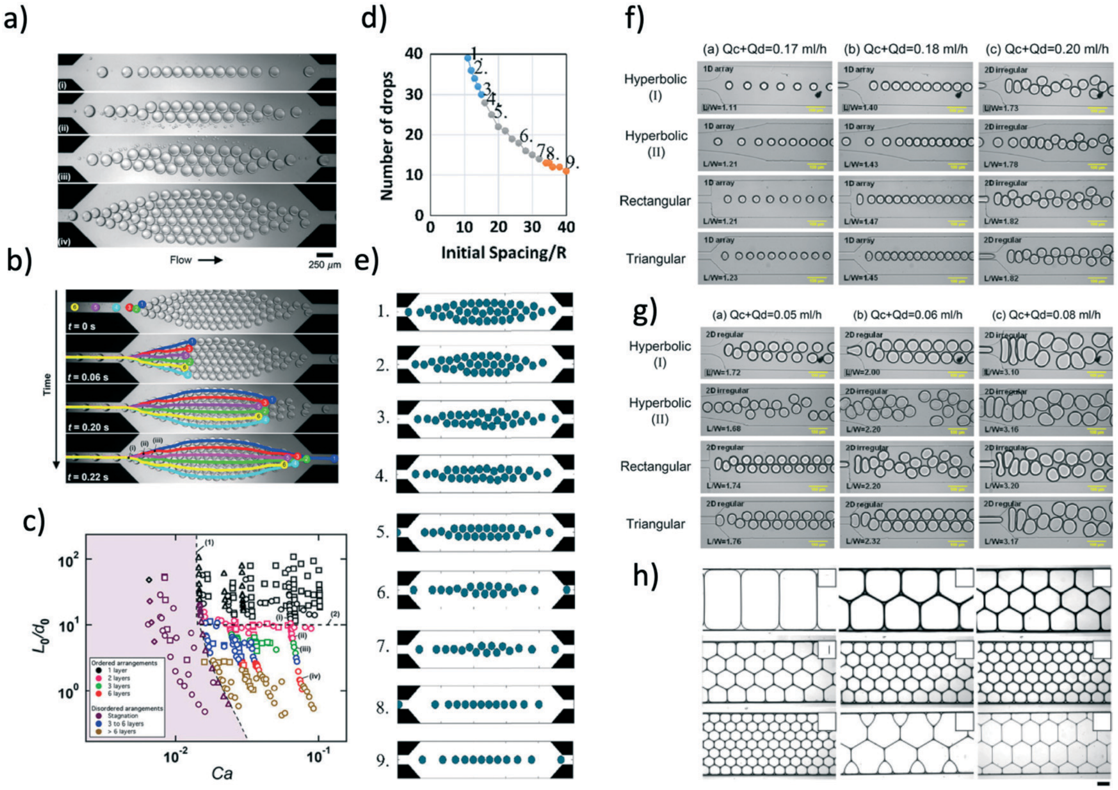

Fig. 3 a) Formation of multiple layers in the microfluidic chamber at different flow rates of the dispersed phase and a constant flow rate of the continuous phase of Q_c = 400 μl min^{-1}: flow rate values of the dispersed phase are Q_d = 14 μl min^{-1} (i), Q_d = 30 μl min^{-1} (ii), Q_d = 40 μl min^{-1} (iii) and Q_d = 85 μl min^{-1} (iv). b) Temporal evolution of the trajectories of six successive droplets in a six-layer arrangement for Q_c = 400 μl min^{-1} and Q_d = 85 μl min^{-1}. c) General phase diagram to obtain droplet crystals with different layouts. L_0 is the distance between consecutive droplets, d_0 is the diameter of the droplet and Ca is the capillary number. Panels a)–c) are reprinted with permission from Springer Nature: *Microfluidics and Nanofluidics*, Droplet arrangement and coalescence in diverging/converging microchannels, Jose and Cubaud,[24] Copyright Springer Nature, 2012. d) Number of drops as a function of the initial spacing between consecutive droplets. e) Numerical snapshots of the crystal configuration resulting from the combination between droplet number and initial spacing. Numbers in (e) refers to the data points in (d). Panels d) and e) are reprinted with permission from Springer Nature: *Microfluidics and Nanofluidics*, Understanding drop-pattern formation in 2-D microchannels: a multi-agent approach, Danny Raj and Rengaswamy,[25] Copyright Springer Nature, 2014. f) Snapshot of droplet crystals generation within microfluidic devices with different funnels for a constant flow rate of the continuous phase equal to Q_c = 0.16 ml h^{-1}. The flow rate of the dispersed phase was regulated as: Q_d = 0.01 ml h^{-1} (i), Q_d = 0.02 ml h^{-1} (ii) and Q_d = 0.04 ml h^{-1} (iii). g) Experimental snapshots as in (f) for a constant flow rate of the continuous phase Q_c = 0.04 ml h^{-1}. The flow rate of the dispersed phase is Q_d = 0.01 ml h^{-1} (i), Q_d = 0.02 ml h^{-1} (ii) and Q_d = 0.04 ml h^{-1} (iii). Panels f) and g) are reprinted with permission from Springer Nature: *Korea-Australia Rheology Journal*, Effect of local kinematic history on the dynamic self-assembly of droplets in micro-expansion channels, Yang *et al.*,[26] Copyright Springer Nature, 2011. h) Optical microscopy images of hexagonal lattices formed by droplets having different volume. Reprinted with permission from Seo *et al.*,[27] Microfluidics: from dynamic lattices to periodic arrays of polymer disks, **21**(11), Copyright 2005, American Chemical Society.

the chamber. The first droplet travelled towards the upper part of the chamber while the second one was deflected on the second row and so on, similarly to the zig-zag 2D crystals observed by Beatus *et al.*[8] and by Fleury *et al.*[10] An interesting consideration is that the droplet confinement in Jose and Cubaud[24] was significantly smaller than the one in Fleury *et al.*:[10] despite such difference, hydrodynamic interactions were still significant and led to the formation of 2D crystals. In other words, even values of the droplet confinement that do not force a significant pancake-like droplet shape are sufficient to generate hydrodynamic interactions aimed at the formation of droplet crystals. Similar results regarding occurrence of hydrodynamic interactions between droplets having different type of confinement can be found comparing the work of Shen *et al.*[28] with the one of Ohmura *et al.*:[29] both works analysed hydrodynamic interactions between two droplets in i) strong confinement[28] and ii) more mild confinement.[29] An important aspect arising from the analysis of Fig. 3a is the occurrence of a transition from 1D-crystal to 2D-crystal formation when changing the flow rate of the continuous phase Q_c. Jose and Cubaud[24] reported a phase diagram linking the crystal formation to both capillary number Ca and frequency of droplet formation expressed as distance between consecutive droplets L_0 normalised by the droplet initial diameter d_0 (*i.e.*, at the flow focusing area), as reported in Fig. 3c. The main message arising from this analysis was that the formation of 1D crystals occurred at low droplet formation frequency values, with $L_0/d_0 \geq 10$: in this case, the first droplet entering the diverging/converging geometry had sufficient time to travel along the axis before another droplet arrived. When increasing the frequency of droplet formation, meaning an increase of Q_d, the flow dipole generated by the first droplet entering the diverging/converging area interacted with the one generated by the upcoming droplets, resulting in a multi-layered 2D crystal configuration. We expect the phase diagram reported in Fig. 3c to be valid only for the geometry described in the corresponding work. A variation of geometrical parameters in the device such as channel height, angle in the diverging/converging chamber are expected to modify the transition between 1D to 2D crystals and also the type of multi-layer crystals observed because of a variation of the hydrodynamic interactions among droplets.[25] While the results by Jose and Cubaud[24] can be qualitatively explained using the same arguments presented in the seminal paper by Beatus *et al.*,[8] a more quantitative analysis has been carried out with the aid of numerical simulations (Fig. 3d and e).[25] The interacting drop-traffic model solved in creeping flow (*i.e.*, at very low Reynolds number values) was employed to describe the different forces acting on droplets flowing in the same geometry of Jose and Cubaud.[24] This model assumes that the droplets are subjected to three forces: i) a force exerted by the continuous phase, ii) a force due to the presence of other droplets when the distance between the two centres of gravity approach the droplet diameter, and iii) the force due to the geometrical boundaries. By solving the resulting equations, the results by Jose and Cubaud[24] were replicated in full (Fig. 3d and e). The authors also demonstrated that droplet crystal configurations observed in the diverging–converging geometry depended upon the frequency of droplet formation, as originally reported by Jose and Cubaud.[24] Specifically, when the initial spacing between consecutive droplet was small, *i.e.*, at large droplet formation frequencies (high throughput), there was a tendency to form 2D crystal-like structures. On the contrary, when the spacing between droplets was large, *i.e.*, at small droplet formation frequencies (low throughput), 1D crystal-like structures were formed. More interestingly, the authors evaluated the resulting crystal-like structures when changing the geometry of the diverging–converging area: they found that the midsection of the microchannel, where the velocity profile was nearly flat along the channel width, had the largest effect on pattern formation rather than the 'shape' of the inlet and outlet of the expansion area. The transition from 1D to 2D crystals as function of droplet size and volumetric flow rates has also been reported in other works.[30–32]

The effect of the shape of the inlet and outlet of the expansion area was experimentally investigated by Yang *et al.*[26] (Fig. 3f and g) using devices with uniform height h = 200 μm. They referred to the different shapes as 'local kinematic history', meaning the history that each droplet experienced before entering the expansion area. For a fixed geometry, an increase of the dispersed phase flow rate Q_d resulted in the transition from 1D crystal-like structures to 2D structures (not necessarily crystals), in agreement with the findings presented previously.[24,25] At variance with previous experimental evidence, though, the 'regularity' of the 2D structure depended upon the kinematic history. With reference to Fig. 3f, 1D structures were all crystal-like regardless of the geometry, whereas 2D crystal-like structures were only observed for the triangular inlet to the expansion area; in all the other cases, at large values of Q_d, the pattern was always irregular, thus preventing the formation of any crystal-like structure. The formation of droplet crystals at low capillary number values was also explored (Fig. 3g). The formation of regular 2D crystal-like structures was only found in devices denoted as hyperbolic (I) (Fig. 3f) or in those with rectangular shape. The aforementioned results show that the geometrical design of the channel has a strong impact on the formation of 1D or 2D crystal-like structures. While a more general framework relating flow parameters to droplet formation in different geometries exists,[3] the same is not true for crystal-like formation due to the complexity of the multi-body system. A comprehensive framework addressing the formation of crystal-like structure would enable deterministic formation of microfluidic crystals, thus opening new opportunities for microfluidic applications.

All the microfluidic crystals introduced so far were made by droplets with a circular cross-section, either in a pancake configuration or in a more spherical shape. In some microfluidic applications such as digital PCR,[17] 2D crystals are organised in the expansion area of the microfluidic device in order to fill in the whole space. Of course, if the 2D crystal is made of circular droplets, there will be empty spaces in the device with consequent reduction of assay throughput. In such circumstances, it would be beneficial to employ 2D crystals made of drops with rectangular or hexagonal cross-section or any other suitable shape that can fill in a rectangular chamber entirely, without leaving empty spaces. Seo *et al.*[27,36] fabricated 2D microfluidic crystals made of different internal shapes, with the aim of forming 2D lattices (Fig. 3h). They observed that by changing the volume of the formed droplets, it was possible to generate2D crystals with pentagonal or hexagonal shapes. They employed silicone oil with viscosities in the range of 0.64 to 50 cP in an aqueous 2 wt% sodium dodecyl sulfate solution; the interfacial tension was γ = 2.71 mN m^{-1}. The imposed flow conditions resulting in a capillary number Ca $\simeq 1 \times 10^{-4}$, meaning very small values of the imposed flow rate (0.1 to 2 μL min^{-1}).

For small values of the droplet volume (0.53 to 1.12 nL), the 2D crystals were made by droplets with a circular shape.[36] When increasing the droplet volume above 1.52 nL, the circular droplets deformed into different shapes (because of the confinement) and filled in the entire chamber, even in the case of bimodal droplet distributions (see the two bottom-left panels in Fig. 3h). The potential formation of 2D crystals fitting the entire expansion area solved the problem of empty spaces caused by spherical droplets. However, shapes different from the circular one in 2D crystals have been generated only for very small flow rate values, which somehow limits the applications to low throughput ones. Even more recent attempts[37] to form honeycomb microfluidic crystals using surfactants with two different adsorption rates were limited by low flow rate values (same range as Seo *et al.*[27,36]); furthermore, the honeycomb structure in Fujiwara *et al.*[37] was not perfectly uniform and changed over time because of the absorption of the second surfactant on the droplet surface. Very recently, the morphology of microfluidic crystals observed by Raven and Marmottant[38] were numerically reproduced[39] using a multicomponent Lattice Boltzmann method augmented by a forcing term representing the near-contact forces at the interface between two droplets.

Until now, we mainly focused on the formation of 1D and 2D crystals. Intuitively, to produce 3D structures, the droplets need to have some ‘free space’ along the height of the microchannel, a condition that has never been fulfilled in the works discussed above. Hatch *et al.*[33] demonstrated the formation of 3D droplet crystals in microfluidic devices (Fig. 4a and b). More specifically, they either changed the flow rate value of both continuous and dispersed phase in order to obtain droplets with diameter smaller than the channel height, or changed the height of the microfluidic device compared to the size of the droplet. By doing so, they demonstrated the transition from 2D to 3D microfluidic droplet crystals. The type of crystals formed depended upon the ratio between chamber height and droplet size, as reported in Fig. 4a. A different approach was followed by Priest *et al.*[34] who employed a step emulsification device (Fig. 4c) to produce 3D crystal lattices made of pentagons (Fig. 4d). They employed water or glycerol water with the addition of 2 wt% of NaCl as dispersed phase and Isopar low viscosity organic liquid with Span 80 as continuous phase. When the droplets entered the ‘step’ in the microfluidic device, they settled because of density difference, thus occupying the floor of the device; additional droplets settled above the ones occupying the floor leading to the formation of 3D droplet crystals (Fig. 4d). A potential disadvantage of the systems employed by Hatch *et al.*[33] and by Priest *et al.*[34] is that the formation of the 3D crystal was delayed by the presence of the continuous phase that needed to be replaced by new droplets. A way around this problem has been proposed by Wang *et al.*[40] and then significantly optimised by Parthiban *et al.*[35] Wang *et al.*[40] simply added some tiny lateral channels to the expansion region with the goal of removing the continuous phase, thus ‘accelerating’ the formation of the 3D droplet crystal. They employed a microfluidic device with constant height h = 50 μm where water-in-oil droplets were formed using a flow-focusing geometry: the droplets then reached an expansion area where strong hydrodynamic interactions took place, facilitated by the removal of the oil *via* the lateral channels. The resulting 3D crystals was not perfectly uniform across the expansion area, thus leaving room for design optimisation. In this respect, Parthiban *et al.*[35] recently demonstrated production of uniform 3D droplet crystals using an expansion area that changed the height gradually from h = 500 μm to h = 2000 μm; before the expansion area, a single lateral channel was used to subtract the continuous phase. With reference to Fig. 4e, the authors demonstrated that when not removing the continuous phase (oil, in their case) water droplets tended to form only 2D microfluidic crystals. When increasing the amount of continuous phase subtracted before approaching the expansion area (meaning a reduction of the distance between consecutive droplets), the droplets arranged to form 3D closely packed microfluidic crystals that were uniform across the expansion area. It is interesting to notice the analogy between the results of Parthiban *et al.*[35] with those of Jose and Cubaud:[24] in both cases a transition between different crystal orders was obtained by reducing the distance between consecutive droplets in order to enhance

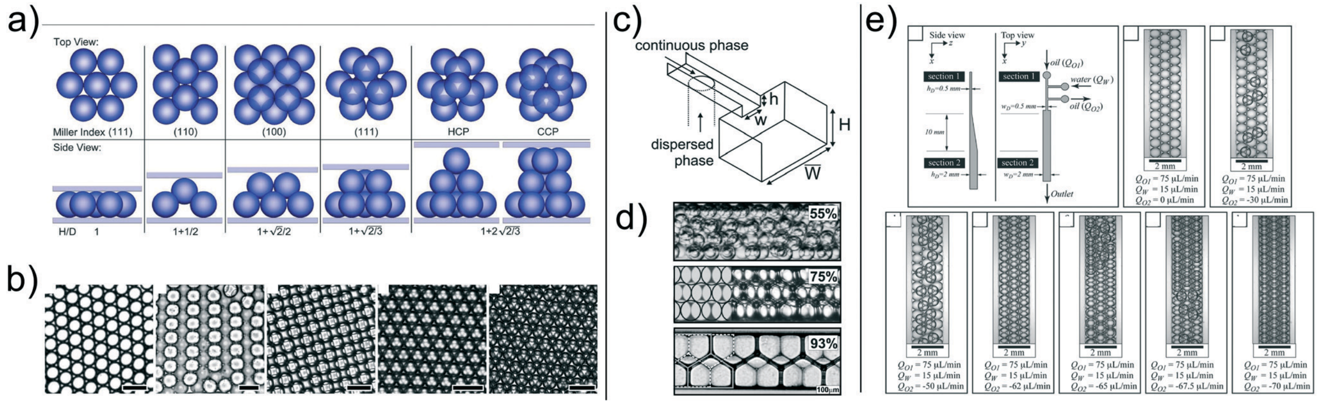

Fig. 4 a) Three-dimensional droplet sphere packing configurations. Illustration of self-assembled droplet sphere packing configurations as a function of chamber height/droplet diameter ratio, *H*/*D*. b) Brightfield images of single layer to triple layer self-assembled droplet sphere packing configurations. Scale bars are 100 μm. Panels a) and b) are reproduced from ref. 33 with permission from The Royal Society of Chemistry. c) Schematic of the single step emulsification geometry, where w = 200 μm, h = 10, 22 or 43 μm, while H = W = 250 μm. d) Self-assembly of gel emulsions in microchannels. As the dispersed phase volume fraction increases (top to bottom), the structural order of the emulsion increases substantially. Panels c) and d) are reprinted from Priest *et al.*,[34] Generation of monodisperse gel emulsions in a microfluidic device, **88**(2), 2006 with permission of AIP publishing. e) Schematic illustration of 3D microfluidic devices used for self-assembly of water droplets into 2D and 3D ordered array. Experimental snapshots of the microfluidic crystals obtained for different volumetric flow rate values of the inlets/outlets. Reproduced from ref. 35 with permission from The Royal Society of Chemistry.

hydrodynamic interactions. Parthiban *et al.*[35] also demonstrated that the kinematic history of the liquid entering the expansion area was important to generate 3D crystals, echoing the results for 2D droplet crystals introduced by Yang *et al.*[26] When using a sudden expansion area (without the gradual change from h = 500 μm to h = 2000 μm), it was not possible to obtain stable 3D crystals, thus further strengthening the argument that the local kinematic history remain a crucial parameter to achieve crystals with a well defined order and regularity.

Before closing this section, we make a final consideration regarding droplet crystals made of droplets having different properties. In applications such as synthesis of anisotropic particles[41,42] or microfluidic crystals[43] formed by polymerised droplets having different properties, it is important to know how to inject the two droplets types in order to obtain the desired final structures. Numerical simulations carried out by Danny Raj *et al.*[44] using the same geometry of Jose and Cubaud[24] studied the effect of the injection policy of two droplets types called 'A' and 'B', obtaining also some counterintuitive results. For instance, they demonstrated that an injection policy ABAB led to a microfluidic crystal where the succession of particles follow the order ABAB only when the crystal was 1D. For 2D droplet crystals with 6 layers (such as those in Fig. 3a) the injection policy ABAB led to a 6 layer crystal where the top 3 layers were formed by droplet A and the bottom 3 layers formed by droplet B. The observed layering (a symmetry breaking instability) was caused by the infinitesimal local perturbations around the droplets entering the expansion channel. The results by Danny Raj *et al.*[44] demonstrated even further the complexity of the formation of crystal-like structures in microfluidic device and called for further studies targeting a general framework to describe the observed structures.

3.3 Applications of droplet crystals

In this section, we discuss some applications of droplet crystals. In the majority of cases, these applications have been characterised as 'droplet microfluidics', thus somehow overlooking the importance of having a crystal-like structures to obtain, for instance, high throughput assays and to avoid cross-contamination in analytical chemistry applications. A notable exception is the commercialised PCR system by Stilla Technologies, which is labelled as Crystal Digital PCR. It is our intention to highlight some recent works in the field where droplet crystals play a crucial role, while we will refer the interested reader to other more comprehensive reviews on the topic at large.

3.3.1 Droplet crystals in analytical chemistry. Droplet crystals can be seen as an ensemble where each droplet occupies a specific place within the ordered structure. Each of these droplets can be also seen as a micro-reactor, where biochemical reactions can take place in parallel. The possibility of running multiple parallel reactions in a single microfluidic crystal has been largely exploited, for instance, for polymerase chain reactions (PCR) applications.[50] PCR is a technique aimed at exponentially amplifying the DNA during three thermal cycles: in the first high temperature cycle (≈95 °C), the two double strands of the DNA are denatured to two single strands. The temperature is then lowered (≈56 °C) for the annealing step where short primers anneal to the targeted DNA. Furthermore, a polymerase (generally derived from *Thermus aquaticus*) attaches to the formed complex. The temperature is finally raised (≈72 °C) during the extension step where the polymerase gains activity and synthesises a second complementary DNA strand from the free nucleotides in solution. Since the PCR is a series of biochemical reactions, it represents the ideal application where microfluidics can contribute: many are, indeed, the microfluidic devices related to PCR analysis (see for instance the reviews by Ahrberg *et al.*,[50] Sreejith *et al.*,[51] and by Yin *et al.*[52]). In the context of droplet crystals for PCR applications, Hatch *et al.*[17] employed a 3D droplet microfluidic crystal introduced in an earlier work[33] to perform PCR in a 1 million droplet array packed in a large chamber (Fig. 5a and b). The droplets were first formed and then split in subsequent smaller droplets using the microfluidic device reported in Fig. 5a. After splitting, the droplets entered a wide chamber having height larger than the droplet diameter, where they self-assembled in a 3D crystal. The droplet crystal presented a coexistence of a (100) square packing and (111) hexagonal packing due to the fact that a slightly mismatch in the ratio between the height of the channel and the droplet diameter led to a different crystal orientation (Fig. 4a). The tightly droplet packing ensured (almost) full filling of the chamber volume thus maximising the throughput. Fluorescent analysis using a conventional DSLR camera was employed to quantify the PCR efficiency, with good agreement observed between experiments and expected outcomes. The thermal cycle was carried out integrating a thermocycle control module located below the microfluidic device. A microfluidic platform for the quantitative and sensitive detections or rare mutations using 1D and 2D droplet crystals has been introduced by Pekin *et al.*[53] The authors employed a flow focusing droplet generator to form 1D droplet crystals: the droplets entered a tapered expansion where they self-assembled in 2D crystals, similarly to those observed by Gai *et al.*[21] The evaluation of the mutations were quantified using fluorescent confocal microscopy. A technological advancement in terms of droplet detection has been presented by Yelleswarapu *et al.*[54] where up to one millions of droplets per second could be analysed using a conventional phone camera. At variance with the work of Hatch *et al.*,[17] they employed flow-focusing droplet generator in parallel aimed at the formation of 1D droplet crystals. As previously discussed, one way to drive the formation of compact droplet crystals is to remove the continuous phase in the expansion chamber.[35,40] By following this procedure, O'Keefe *et al.*[45] employed a microfluidic chamber with an intermediate sieve layer having a twofold function: i) remove the continuous oil phase to

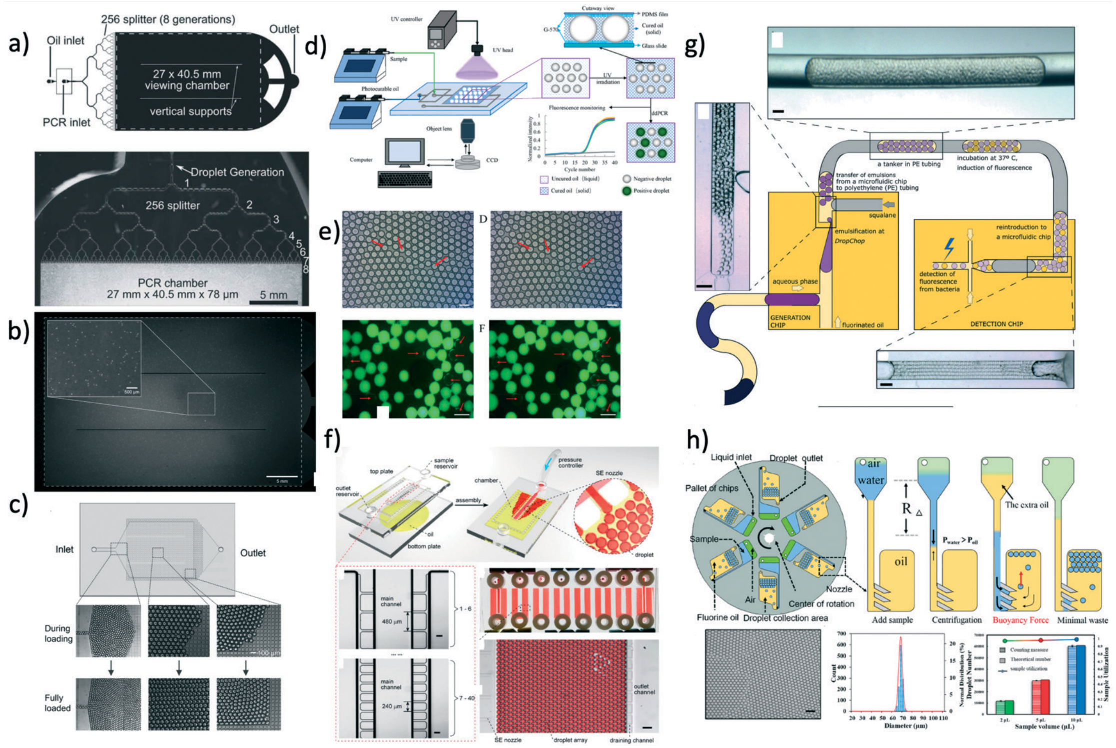

Fig. 5 a) Schematic of the microfluidic device with 256 splitting parts used to generate 1 million droplets in few minutes. b) Image of the fluorescent signal derived from the PCR analysis occurring in the microfluidic crystal. Panels a) and b) are reproduced from ref. 33 with permission from The Royal Society of Chemistry. c) Droplets are self-assembled with the help of a grid where the continuous phase is filtered. Upon removal of the continuous phase, the crystal self-assemble in a uniform 2D droplet crystal. Reprinted with permission from O'Keefe *et al.*,[45] Highly efficient real-time droplet analysis platform for high-throughput interrogation of DNA sequences by melt, *Analytical Chemistry*, **91**, 17, 11275, Copyright 2019, American Chemical Society. d) Droplets are 'frozen' in space by curing the photocurable oil (continuous phase) using a UV lamp. This approach prevented coalescence during the PCR thermo cycle. e) Experimental snapshots of the 2D droplet crystal before (left) and after (right) the PCR thermo cycle. Top and bottom image refer to the fluorescence signal obtained before (left) and after (right) 40 PCR cycles. Panels d) and e) are reprinted with permission from He *et al.*,[46] Rapid *in situ* photoimmobilization of a planar droplet array for digital PCR, *Analytical Chemistry*, **92**, 8530, Copyright 2020, American Chemical Society. f) Schematic of the step emulsification droplet PCR device. At variance with other microfluidic device, here the droplet are formed by employing only a single syringe pump with the continuous phase being preloaded in the device. This arrangement leads to the formation of 2D droplet crystals. Reprinted with permission from Nie *et al.*,[47] Assembled step emulsification device for multiplex droplet digital polymerase chain reaction, *Analytical Chemistry*, **91**, 1779, Copyright 2019, American Chemical Society. g) Schematic of the experimental setup to generate droplet tankers each containing droplet crystals. Reproduced from ref. 48 with permission from The Royal Society of Chemistry. h) Schematic of the centrifugal-driven droplet generation. The centrifugal force pushes the water (dispersed phase) through the oil (continuous phase): this is similar to a step emulsification device where the syringe pump is replaced by the centrifugal-driven flow. Scale bar in the experimental snapshot is 200 μm. Reprinted with permission from Li *et al.*,[49] Centrifugal-driven droplet generation method with minimal waste for single-cell whole genome amplification, *Analytical Chemistry*, **91**, Copyright 2019, American Society of Chemistry.

enhance the formation of a 2D crystal and ii) immobilise each droplet in a single place (Fig. 5c). By using this device, the authors demonstrated real-time analysis of individual droplets to detect heterogeneous DNA methylation of the CD01 tumour suppressor gene using PCR analysis followed by a digital high resolution melt analysis (a post-PCR procedure aimed at identifying sequence variations in DNA).

During the PCR cycle, the reagent needs to undergo different thermal cycles where the temperature is changed significantly with $\Delta T \approx 40$ °C. Such abrupt temperature change affects the integrity of the 3D crystal-like structure, as the droplets tend to coalesce.[17] From an application point of view, droplet coalescence means cross-contamination among different micro-reactors. A solution to this problem was proposed by Bian *et al.*[55] that employed a microfluidic device made of polydimethylsiloxane (PDMS) saturated with mineral oil on a silicon mould fabricated using conventional lithography. This step was critical to avoid droplet evaporation under many rounds of thermal cycling, thus preserving the integrity of their 2D crystal, meaning larger throughput and no cross-contamination. They also employed two-colour fluorescent probes for simultaneous detection of *E. coli* O157:H7 and *L. monocytogenes*. A different approach aimed at overcoming the problem of coalescing droplets has recently been introduced by He *et al.*[46] They employed a flow-focusing droplet formation technique to create a 2D droplet crystal made of polyurethane droplets (dispersed phase) in photocurable oil (continuous phase). By using a UV lamp, they polymerised the oil surrounding the droplets, thus 'freezing' the 2D crystal (Fig. 5d and e). This technique remains valuable to avoid droplet coalescence during PCR thermocycle but also to prevent droplet free movements, thus making real-time analysis possible without the use of a sieve as presented by O'Keefe *et al.*[45] By using this technique, highly efficient PCR fluorescent readout was demonstrated. We expect that a further improvement in terms of throughput can be realised by creating a 3D crystal structure in the PCR chamber rather than a 2D crystal. Of course, there are some foreseeable challenges associated to the formation of the 3D crystals during photopolymerisation process. Apart from direct PCR applications, 2D droplet crystals have also been recently employed to detect cancer biomarkers[56] and circulating tumour DNA.[57] Similar considerations remain regarding increasing the assay throughput by adding an extra dimensionality to the crystal, from 2D to 3D.

In all the applications presented so far, the formation of droplet crystals occurred after the formation of individual droplets using either a T-junction geometry or a flow-focusing geometry. However, this often requires very sensitive control of the applied volumetric flow rate in order to obtain uniform droplets that can then self-assemble in a droplet crystal. This problem has been addressed firstly by Xu *et al.*[58] that generated droplets by using a microfluidic device with a single inlet, leading to a rectangular channel with aspect ratio larger than 3.5 followed by an expansion area (this technique was named 'step emulsification'). The expansion chamber of the microfluidic device was first filled with the continuous phase (oil); the dispersed phase (water) was then pumped *via* the single channel and, upon reaching the expansion, it formed a droplet that was pinched off because the equilibrium Laplace pressure acting on the droplet could not be maintained thanks to the abrupt expansion. The authors employed this technique to perform PCR analysis aimed at identification of the targeted genomic DNA purified from lung cancer lines H1579. This concept has been also recently pushed further by Nie *et al.*[47] that designed are usable multiplex microfluidic device for PCR analysis in 2D droplet crystals (Fig. 5f). The device was made of two soda-lime glass plates patterned by standard photolithography and wet chemical etching techniques. The two pieces of glass were simply bonded using binder clips: after each use, the device could be easily cleaned and then reused. The oil (continuous phase) was pre-loaded in the microfluidic device before clamping the two pieces of glass. Then, the dispersed phase was injected using a single inlet that ended in several lateral channels with different diameters: when the dispersed phase was in contact with the oil, droplets were formed as for the step emulsification technique described by Xu *et al.*[58] Moreover, the formed droplets interacted forming a 2D droplet crystal: together with an additional parallelisation (eight parallel channels), the authors achieved a very large throughput. They employed this device to detect template DNA at concentrations as low as 10 copies per μL and they also performed quantitative assessment of HER2 copy number variation, important for targeted therapy and prognosis of breast cancer.

The majority of droplet crystals employed for PCR applications, either 2D or 3D, were very valuable for the analysis of a single sample *via* droplet parallelisation. A different approach is needed when a simultaneous analysis of different samples is required. An example is the evaluation of the minimum inhibitory concentration (MIC), meaning the lowest concentration of antibiotic in which the growth of bacteria cannot be observed. The MIC strongly depends upon the initial bacteria concentration, and such phenomenon is called inoculum effect (IE). The IE is very important in the clinical practice because it can lead to an overestimation of the MIC *in vitro*, thus causing an increased mortality among patients. To correctly evaluate the MIC, analysis with different amount of antibiotics are required, thus making the devices introduced so far not optimal unless when using several of them in parallel. In an attempt to solve this problem, Postek *et al.*[48] recently employed a microfluidic system for the formation of droplet tankers each containing a 3D droplet crystal (Fig. 5g). The authors first prepared off-chip microliter mother droplets, each with a different chemical environment. The droplets were then aspirated from a well plate with emulsification taking place using the Drop Chop device introduced previously by the same authors.[59] These droplets were then injected in another channel where they were encapsulated in a larger droplet called tanker using immiscible squalene (Fig. 5g). Once within the tanker, the encapsulated droplets self-assembled in a 3D microfluidic crystal that was then subjected to incubation at 37 °C while flowing in a tube, and then re-injected in the microfluidic device for detection. Since the mother droplets were all presenting different chemical environments, it was possible to simultaneously run MIC assays. Another advantage of the approach employed by the authors is that each reactor tanker contained a 3D droplet crystal, meaning a very large amount of individual micro-reactors in parallel, thus making the whole procedure high-throughput. In terms of stability of the 3D droplet crystal within the tanker, no significant variation in droplet number and shape after 16 hours at 37 °C was reported. However, follow up studies should analyse the effect of large temperature differences (such as those experienced during PCR) on the stability of the tanker, in order to expand the range of applicability of this platform.

The advent of step emulsification droplet formation using a single channel opened the way to a different approach for droplet formation where the motion of the dispersed phase was not imposed by an external syringe pump but rather by the centrifugal force experienced by the fluid during the 'spinning' of the microfluidic device. Centrifugal step emulsification was employed by Schuler *et al.*[60] to produce individual droplets that then self-assembled in a 2D crystals made of hexagons, where recombinase polymerase amplification (RPA), *i.e.*, a DNA amplification technique occurring at the constant temperature of ~39 °C, took place. In a successive work,[61] the authors also performed PCR on a disk using a centrifugal step emulsification technique to form 2D crystals. The 2D crystal was formed by changing the speed of the centrifuge in order to change the balance between centrifugal and capillary forces: air bubbles were then removed using a bubble drain, thus allowing formation of a large 2D crystal occupying the whole PCR readout area. A similar result was also obtained by Peng *et al.*[62] who designed a microfluidic device with an oil-storage structure for the regulation of the thickness of the oil film (continuous phase) between neighbouring water droplets. An example of parallelisation of microfluidic devices subjected to centrifugal force has recently been presented by Li *et al.*,[49] who performed PCR analysis with 98% of sample utilisation as well as a single-cell whole genome amplification. With reference to Fig. 5h, oil was first added to the device followed by water and air. During centrifugation, water droplets were formed in the continuous oil phase; to minimise the waste, additional oil used to push the remaining water to form other droplets in oil was added. The advantage of this approach was that more droplets could be formed, thus leading to strong hydrodynamic interactions which formed a uniform 2D crystal for both PCR and whole genome analysis. Some limitations encountered in centrifugal microfluidic for the formation of droplet crystals include the possibility of controlling droplet size and droplet formation without changing the rotational speed. As extensively discussed, the injection policy may alter the dimensionality of the microfluidic crystal,[24] while the possibility of changing the droplet size compared to the height of the microfluidic device can lead to a reacher variety of droplet crystals.[33] The first problem has been addressed by Wang *et al.*[63] who designed a centrifugal microfluidic pressure regulator scheme to control droplet formation without changing the rotational speed. Specifically, they employed an air chamber as pressure regulator to control the droplet crystal formation. The second problem has been recently addressed by Clime *et al.*[64] who employed pneumatic actuation for fluid displacement. They demonstrated formation of uniform 2D droplet crystals, each having individual droplets with different diameter and narrow standard deviation.

Before concluding this section, we want to highlight a recent work by Kao *et al.*[65] where the microfluidic crystal was formed without the support of any type of external flow equipment, nor syringe pump, nor centrifugal force. The device was still based on the step emulsification process where the continuous phase was, as usual, added in the droplet generation chamber; moreover, the dispersed phase as well was added to a reservoir in the microfluidic device using a pipette. The flow was then initiated by orienting the device vertically, with the gravity driving the dispersed phase in the continuous phase chamber, thus leading to the formation of droplets that then self-assembled in 2D crystals. The same device was used for digital enumeration of bacteria and for antibiotic susceptibility testing. We believe that similar approaches will be required in the future in the attempt to use microfluidic devices in places where expensive pieces of equipment are not available.

3.3.2 Droplet crystals in colloidal fabrication.

The fabrication of colloidal structures using microfluidic devices has attracted an enormous interest.[16,68,69] As for the biochemical applications previously described, the fabrication of colloids currently falls in the field of droplet microfluidics. It is our intention here to highlight a more recent research direction that is currently gaining momentum based on the fabrication of colloidal crystal-like structures by taking advantage of the hydrodynamic interactions among droplets discussed before. Even though there are not many existing works in this field, we envisage many future works where hydrodynamic interactions will play a key role in the fabrication of droplet crystals.

So far, we discussed findings related to the formation of droplet crystals having either different dimensionality (1D, 2D, 3D) or having individual crystal components with different shape (circle, hexagon, pentagon, *etc.*). However, while such crystals have been advantageous in analytical chemistry, they find limited interest when seeking to fabricate small colloidal crystal-like structures. Shen *et al.*[66] presented the first experimental evidence of formation of colloidal crystal-like structures resulting from the hydrodynamic interactions of the single droplet units (Fig. 6a and b). They employed a microfluidic device with two different heights, in analogy with the aforementioned step emulsification geometry. In the first part of the channel, droplet plugs were formed using a flow-focusing geometry; when entering the wider chamber with larger channel height, the plug dissociated in different circular droplet units. After adding a large amount of surfactant, far above the critical micellar concentration, the so-formed droplets remained in contact and began to interact hydrodynamically to form a variety of colloidal structures depending on the initial configuration of the separated droplets (Fig. 6b). The authors were also able to solidify the formed structures by using acrylate-based polymers and by adjusting the solubilities so that the polymerisation could occur in both continuous and dispersed phase. The potentiality of this approach is that colloidal crystals with different shapes or properties could be easily fabricated with a throughput of up to 30 000 structures per hour. Shen *et al.*[66] suggested the potential of fabricating photonic materials by reducing the dimensions of the individual droplet size down to 400 nm and below. This hypothesis has recently been explored further by Morozov and Leshansky,[70] who suggested to encapsulate the colloidal crystals formed by Shen *et al.*[66] in a droplet, and then use hydrodynamic interactions among droplets to generate different crystals, by using a modified version of the setup by Postek *et al.*[48] Morozov and Leshansky[70] demonstrated numerically the emergence of the omnidirectional band gap in the cubic face centred (fcc) lattice dumbbells. They also reported that encapsulating tetrahedrons over fcc-templated dumbbells caused a reduction of the photonic properties. The results by Shen *et al.*[66] remain, to the best of our knowledge, the only experimental data on the subject. More recently, numerical simulations[67,71] have been carried out to

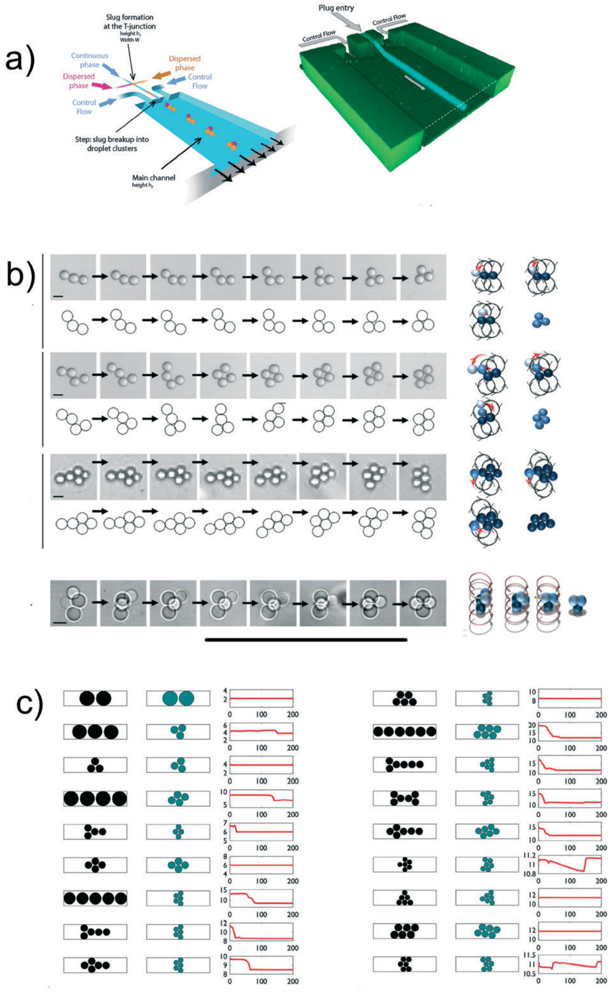

Fig. 6 a) Schematic of the two-level microfluidic device (left) and confocal image of the system taken over long exposure times and comparison with numerical simulations (right). b) Rearrangement kinetic of several crystals with different initial configurations. Top panels are experimental snapshots with scale bar of 50 μm, while the bottom panels are obtained from numerical simulations. Panels a) and b) are reprinted from Shen *et al.*[66] c) Structure configuration observed by Shen *et al.*[66] and used as initial conditions for the numerical simulations by Danny Raj *et al.*[67] (first column). Numerical simulation results outlining the equilibrium conditions resulting from a slight perturbation of the initial conditions (second column). Evolution of the form factor Φ_d defined in the text (third column). Reprinted from ref. 67, with permission of the Royal Society of Chemistry.

replicate the experimental results of Shen *et al.*[66] Ge *et al.*[71] employed confined simple shear and Poiseuille flow as reference flows and showed that the crystal formation is mostly affected by the shear-induced cross-stream migration as long as attractive forces between droplets are present. The Poiseuille flow approximation is valid in 3D flow, meaning that the droplets do not ‘feel’ the presence of the walls and do not assume a ‘pancake’ shape: in such conditions, depletion forces between droplets are more relevant than the long-range dipolar interactions.[67] The results by Ge *et al.*[71] clarified that the crystal formation was a result of hydrodynamic interactions in 3D flow, but they did not provide a predictive framework that would allow crystal design *a priori*. Some steps in this direction have been made by Danny Raj *et al.*[67] They first performed numerical simulations to evaluate the stability of the crystal-like structures introduced by Shen *et al.*[66] (Fig. 6c). At time zero, the droplet configuration was the one by Shen *et al.*[66] (first column in Fig. 6c); after a local perturbation, they studied the variation over time of the structure (second column in Fig. 6c), and quantified the modification using the structure parameter Φ_d (third column in Fig. 6c). Besides the mathematical definition of Φ_d (not reported here), the meaning of this parameter was that structural changes of the colloidal structure were reflected in a change of the Φ_d value. With reference to Fig. 6c, it is clear that there are some structures that are stable over time, while others evolve into a different crystal. Under an experimental point of view, this means that the design of the microfluidic device needs to account for the residence time of the desired crystal. If a metastable configuration is desired, optimisation of the channel design and photo polimerisation time is crucial to achieve the desired crystal. The authors also attempted to introduce a general framework based on the optimisation analysis, solving a large combinatorial problem after fixing a suitable objective function. By doing so, they obtained a non-trivial relation among channel geometry, injection policy, and the resulting geometry; however, their results could not be generalised in a unified framework due to the complexity of the original problem. We agree with the authors that the introduction of machine learning techniques can actually be able to transform the current problem in a deterministic one, where a desired crystal configuration can be achieved by using a specific channel design coupled to a specific injection policy. Future experimental and numerical works are still required to provide a unified framework of action to fabricate microfluidic crystals using hydrodynamic interactions among droplets.

4 Particle crystals

We now proceed to review crystal-like structures made of rigid particles. The most important difference between droplet and particle crystals is the way they are obtained. While the formation of droplets can be accurately controlled in a variety of microfluidic geometries,[3] the same is not true for rigid particles. In other words, the interactions among droplet crystals can be controlled at the micrometer level, while the interactions among rigid particles depend upon their position along the microchannel cross-section and their mutual distances. The spatial distribution of the suspended particles cannot be controlled during the injection process, being the latter a random process. A way to manipulate the position of the particles along the channel cross-section is to exploit non-linear forces such as *inertial* and *viscoelastic* forces. Indeed, both forces are able to drive the flowing particles towards specific equilibrium positions depending on the channel geometry, flow rate, and properties of the suspending liquid, as well documented in several reviews.[72–78] Once the particles reached the equilibrium position, at sufficiently large concentrations, they begin to interact, possibly leading to the formation of crystal-like structures. In this stage, the overall dynamics depends upon the mutual distance between all the interacting particles. This results in a complex collective motion even for the simplest case of an inertialess Newtonian fluid where pairing instabilities, cascades of pair-switching events, propagation of displacement waves occur.[8,9,79,80] These phenomena prevent the formation of equally-spaced structures. On the other hand, inertia or viscoelasticity introduce strong non-linearities that, at some extent, might lead to a stable ordered microstructure. As a result, particle crystals can either be formed on a single fluid line (1D crystals) or on multiple flow lines (2D crystals), and they find several applications in particle/cell encapsulation, flow cytometry and material science, as described in section 5.

In the following sections, we review the self-assembly of particles suspended in a fluid flowing in a microfluidic device induced by inertial or viscoelastic effects. We begin from the dynamics of a particle pair, that is the starting point to understand the particle–particle hydrodynamic interactions. The analysis is then extended to the more complex phenomenon of train formation with a focus on the capability of inertia or viscoelasticity to form stable ordered structures and the effect of the relevant parameters on the particle microstructure.

4.1 Inertial ordering

Before presenting the recent advancements in inertial ordering, it is worth to briefly mention the inertial particle focusing

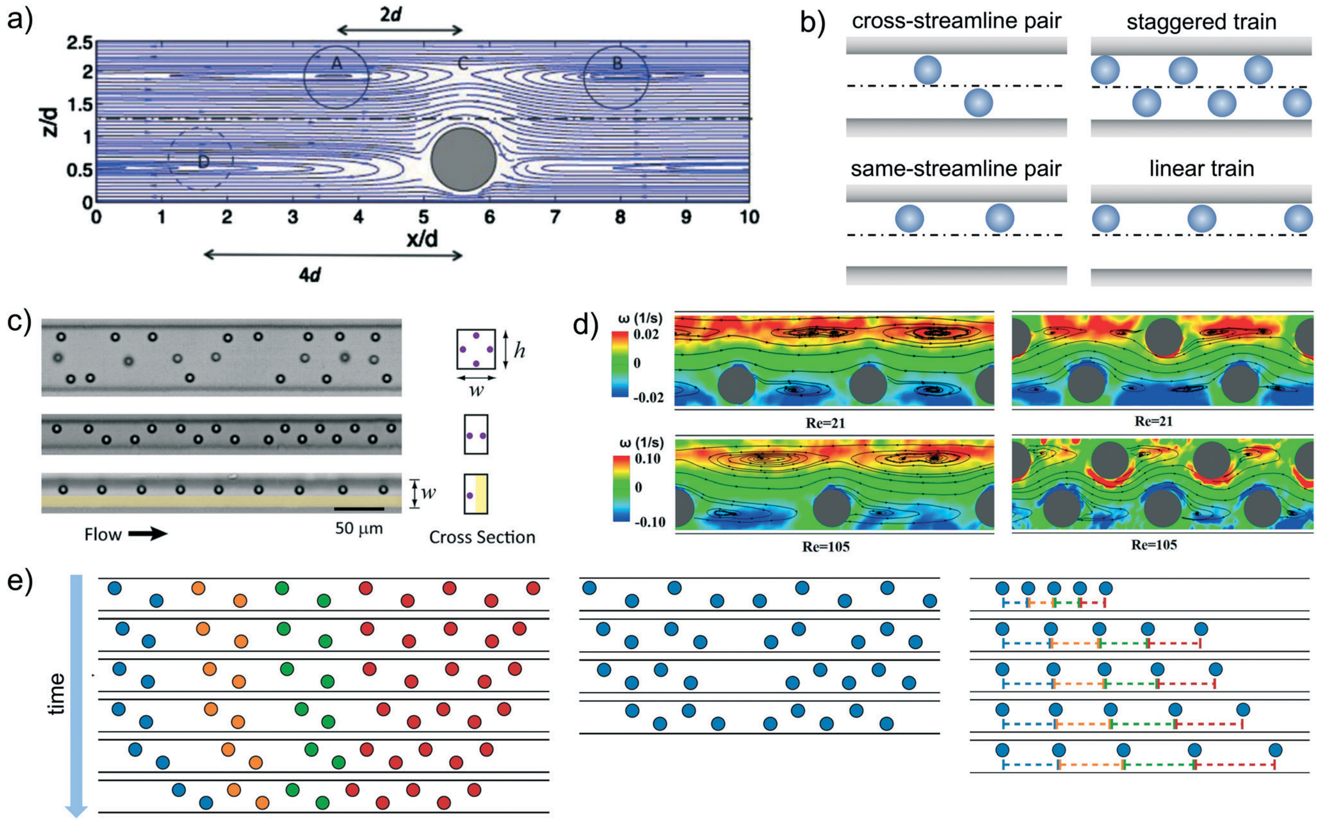

Fig. 7 a) Streamlines around an isolated particle in the flow-gradient plane computed by numerical simulations. The solid and dotted circles suggest the equilibrium positions of adjacent particles. The channel has a rectangular cross-section 4 × 2.5 particle diameters and the particle Reynolds number is 1.25. Reprinted from Humphry *et al.*,[81] Axial and lateral particle ordering in finite Reynolds number channel flows, *Physics of Fluids*, **22**, 081703, 2010, with the permission of AIP publishing. b) Schematic representation of the cross-streamline and same-streamline pair configurations, and staggered and linear trains. c) Visualization of particle microstructure in a square-shaped microchannel with four equilibrium positions (top panel), a rectangular microchannel with two equilibrium positions (middle panel), in a rectangular microchannel with a coflow of a particle-free fluid that confines the particles on one side of the channel resulting in a single equilibrium position (bottom panel). Reprinted with permission from Lee *et al.*,[82] Dynamic self-assembly and control of microfluidic particle crystals, *Proceeding of the National Academy of Science*, 2010, **07**(52), 22413. d) Microscale flow structures around in-line (left) and staggered (right) particle trains obtained from micro-particle image velocimetry experiments at Re = 21 and Re = 105 on the middle plane of a rectangular microchannel. The streamlines of fluid flow relative to the particles are plotted with background contours indicating the vorticity magnitude. Reprinted from Pan *et al.*,[83] Direct measurement of microscale flow structures induced by inertial focusing of single particle and particle trains in a confined microchannel, *Physics of Fluids*, **30**, 102005, 2018, with the permission of AIP publishing. e) Evolution of staggered (left), staggered with defect (middle), and linear particle trains in time obtained by numerical simulations. Reprinted from Schaaf *et al.*,[84] Particle pairs and trains in inertial microfluidics, *The European Physical Journal E*, **43**, 2020.

phenomenon. Particles suspended in a Newtonian fluid and flowing in a straight microchannel under inertial flow conditions experience a combination of forces which result in a net lift force F_L quantified as $F_L = f_L \rho u^2 d_p^4 / D_H^2$, where f_L is a net lift force coefficient, u is the average flow velocity, d_p is the particle diameter and D_H is the hydraulic diameter. A full description of the inertial focusing process, which depends among several parameters, falls outside the scope of this review. In general, particles will migrate towards a variety of equilibrium positions depending upon the Reynolds number and the geometry of the microchannel. We refer the interested reader to the recent review by Tang *et al.*[85]

4.1.1 Particle pair. An isolated particle placed at some arbitrary position on the cross-section of a microfluidic channel at a Reynolds number larger than unity migrates towards an equilibrium position displaced from the midplane.[81] The streamlines around the particle are characterized by two inward spiraling regions on the other side of the channel (denoted by A and B in Fig. 7a), suggesting that a second neighboring particle would move to the centers of the spirals. Such a particle, in turn, disturbs the flow field generating a spiral in the opposite half channel (denoted by D in Fig. 7a) where another particle would migrate, forming a train of 'staggered' particles (Fig. 7b). Numerical simulations of a particle pair located near the inertial focusing equilibrium positions and separated by a certain distance showed that the axial separation distance reached an equilibrium value after a transient dynamics characterized by damped oscillations.[81] This behavior was further supported by an asymptotic theory developed to describe pairwise interactions,[86] showing a similarity between the pair dynamics and a damped spring. The damping effect was related to inertial forces, whereas the spring force was due to the interplay of viscous forces arising from particle–particle and particle–wall interactions.

The stability of staggered particle pairs was also confirmed by detailed numerical simulations.[84,87,88] The particles attracted each other over large distances without significant changes of the cross-stream position. Specifically, depending on the initial lateral positions and axial distance, four different kinds of trajectories were possible.[88] If the leading particle was closer to the channel midline than the trailing one, it travelled faster and the two particles separated, migrating independently towards the inertial equilibrium position up to reach a distance so that they did not interact anymore. A second scenario occurred when the distance between the trailing particle and the channel midplane was much lower than that between the leading particle and the midplane. In this case, the trailing sphere travelled faster and overtook the leading one. Due to the strong hydrodynamic interactions, the particles were displaced along the cross-stream direction and the trailing sphere passed the leading one, and then separated. A third kind of dynamics was observed when the trailing sphere was again closer to the channel midplane than the leading one but the two distances were more similar. In this case, the faster trailing particle approached the leading one without passing. The strong hydrodynamic interactions determined a swapping of the lateral position, making the leading particle faster and the pair separated. Obviously these three scenarios do not lead to a stable configuration. In a range of initial positions where the distances between the two particles and the midplane was similar, the particles followed damped oscillatory trajectories up to reach an equilibrium position. The axial distance was about four times the particle radius, and it was independent of the initial particle positions and the Reynolds number.

The stability of a linear particle pair, *i.e.*, the two particles are aligned along the same streamline of the flow field (Fig. 7b), is less clear. Numerical simulations showed that two aligned particles form a stable configuration with a preferential distance of 5 and 2.5 times the particle diameter at low and high particle Reynolds number, respectively.[89] The stability of a same-streamline pair was also confirmed by the theoretical analysis of Hood and Roper[86] and explained in terms of minimization of the fluid kinetic energy. In contrast, more recent numerical works did not find any stable fixed point in a linear particle pair.[84,87,88] The two particles moved away one to each other up to reach a distance such that the hydrodynamic interactions vanished. This behavior was also observed in experiments where the interparticle spacing increased as the pair travelled along the channel.[82] Detailed experiments have been recently performed in an oscillatory flow field aimed at increasing the distance travelled by the particles using a relatively small microchannel length.[90] Both staggered and linear pairs were considered. In the former case, pair formation quickly occurred when the interparticle spacing reached a critical value, and the equilibrium configuration was very robust against external perturbations. Furthermore, a variation of the line concentration (defined as the particle diameter times the number of particles in the field of view and divided by the length of the field of view) did not affect the equilibrium distance. In contrast, the linear pair formed gradually and the interparticle distance fluctuated as the two particles travelled along the channel. In this same-streamline arrangement, the shape and the mean value of the interparticle spacing distribution strongly depend on the line concentration: lower concentrations spread out the distribution and move the peak towards larger distances.

4.1.2 Particle trains. The formation of trains induced by inertia was observed for the first time by Segré and Silberberg[91] and analyzed in a more systematic way by Matas *et al.*[92] in a macroscopic channel. Strings of aligned and equally-spaced particles located at the Segré–Silberberg radial equilibrium position started to form at a Reynolds number of 100 with just few particles. The number of particles in the train increased with increasing Re, achieved a maximum, and then decreased. Longer trains were observed in more confined flows, motivating the successive studies in microfluidic devices. In microfluidic channels with rectangular cross-section, inertia drives the particles to focus on two equilibrium positions along the symmetry plane identified by the short side of the cross-section.[73] In these channels, a sequence of particles arranged in staggered and linear configuration was observed (see middle and bottom panels of Fig. 7c).[89,93,94] The spacing between staggered particles was about one-half as compared to a linear arrangement. Train formation was a slow phenomenon[95] and occurred through a series of self-assembly phenomena of pairs of particles.[82] Once two or more particles arranged in an organized structure, other particles joined remodulating the distances between the particles of the train.[82,95] During the self-assembly, oscillations of the interparticle distances were observed similarly to the particle pair, denoting an analogy between the hydrodynamic interactions between particles of the pair and the train.[82] The mechanism leading to train formation was explained through the interplay between inertial and viscous effects: inertia drives the particles to the equilibrium position and repulsive viscous effects stabilize the train setting the interparticle spacing. In a square-shaped microchannel, the equilibrium positions induced by inertia are four and are located in the middle of the cross-section sides.[73] Trains of particles are then formed along these streamlines (top panel of Fig. 7c).[95] Experimental observations suggested that trains formed only once the particles reached the equilibrium positions. The analysis of trains made of a limited number of particles showed interesting features. In agreement with Matas *et al.*,[92] the percentage of particles forming the train increased with the particle Reynolds number up to a maximum and then decreased. A similar trend was found for the focusing efficiency, *i.e.*, the percentage of particles focused at the equilibrium positions. Hence, the reduction of the percentage of particles forming a train at high particle Reynolds numbers could be justified considering that a lower number of particles were located at the equilibrium positions reducing, in turn, the probability for these particles to join the trains. A similar behavior was also found for bidisperse particle trains where the percentage of particles in a train was enhanced as compared to the monodisperse case due to the higher stability of pairs made of a small and a large particle.[96] The distance between consecutive particles decreased as the particle Reynolds number increased regardless of the particle concentration. A relatively good agreement between various experimental and numerical results[81,82,92,93,95] was found when the normalized particle surface-to-surface spacing was plotted as a function of the particle Reynolds number, suggesting that the distance between the particle surfaces is the relevant parameter that affects the interparticle spacing. However, for more confined flows, the trend of the interparticle distance as a function of the Reynolds number reverted,[83] highlighting that the confinement ratio is a relevant parameter to determine the particle microstructure. A visualization of the flow field (left panel Fig. 7d) suggested that the vortex between two consecutive particles enlarged at higher Reynolds numbers pushing the particles at a larger distance.[83] In contrast, for a staggered configuration (right panel Fig. 7d), by increasing the Reynolds number one of the two vortices visible at low Re was suppressed and the particles came closer.

Regarding the stability of the trains, both experimental and numerical results confirmed that a staggered configuration is stable[83,84,87,97] in line with the pair particle dynamics. Numerical simulations on a regular staggered configuration (left panel of Fig. 7e) and on a train with all the particles in a staggered arrangement except two middle particles that are placed on the same streamline (middle panel of Fig. 7e) clarified the train formation dynamics.[84] In the case of a regular staggered structure with initial distances higher than the equilibrium one, the train contracts starting from the front and back in a non-uniform way, leading to a 'cascade' of pair formation. The overall velocity of a cluster of staggered particles is lower than that of isolated particles or pairs due to a reduction of the viscous drag, allowing the joining of isolated particles to the train. Regarding the case of a staggered configuration with two middle particles on the same line, the two particles increase their distance and the two parts of the train contract. Once the two small trains achieve the equilibrium configuration, the following dynamics depends on how many particles form the two trains. If the trailing train is made of less particles than the leading one, the latter is slower due to the enhanced viscous drag reduction and the trailing one joins. The equilibrium distance between the two in-line particles is about twice the axial distance between the staggered particles in agreement with experimental observations.[93,94] An opposite scenario occurs if the trailing train has more particles than the leading one. In this case the trailing train moves faster and the two trains separate.

As for the particle pair, the available results assessing the stability of linear trains are controversial. Simulations reported that only linear trains formed by a limited number of particles were stable, where this number was between 2 and 4 depending on the particle Reynolds number and the confinement ratio.[98] Numerical simulations with several aligned particles confirmed (right panel of Fig. 7e) that the interparticle spacing progressively increased without reaching a stable configuration.[84,97] On the other hand, stable linear trains were observed in experiments.[89,95] It has to be pointed out, however, that the train dynamics computed by numerical simulations[84] showed an initial fast variation of the interparticle distances up to a value of about twice the distance between consecutive particles in a staggered configuration in line with experimental observations.[89] In the second stage, the particles continued to drift apart from each other at a much lower rate, making the separation dynamics hardly detectable through experimental observations. Interestingly, the distribution of the particle spacing in random linear trains well reproduced the experimental one,[89] confirming the robustness of the numerical predictions.

4.2 Viscoelastic ordering

Before presenting the recent advancements in viscoelastic ordering, we briefly describe the viscoelastic particle focusing phenomenon. When the viscoelastic suspending liquid presents a near constant-viscosity, particles migrate transversally to the flow direction towards the centreline of a circular or square-shaped channel with a migration velocity given by[78,102] $V_M \sim d_p{}^2\nabla\dot{\gamma}/\eta$, where η is the fluid viscosity, d_p is the particle diameter and $\nabla\dot{\gamma}$ is the shear rate gradient along the channel cross-section. When particles are suspended in a near constant-viscosity liquid, the direction of the particle migration does not depend upon the particle diameter, meaning that the particles will always migrate towards the centreline of a circular or square-shaped straight microchannel.[75,78,103] When the viscoelastic suspending liquid presents shear-thinning features (*i.e.*, the viscosity decreases with increasing the shear rate $\dot{\gamma}$), it was found[104,105] that particles migrate towards the centreline of a square-shaped microchannel only if $\beta \geq 0.2$, while migrating towards both the centreline and the four corners of the channel when $\beta \leq 0.2$ (for a cylindrical geometry, the four corners are replaced by the circular walls). In the case of shear-thinning suspending liquids, there are no explicit expression relating the migration velocity to the properties of the suspending liquids. The interested reader can find more details regarding viscoelastic focusing in the recent review by Zhou and Papautsky.[78]

4.2.1 Particle pair and triplet. The simplest case of two spherical particles suspended in a viscoelastic fluid and aligned at the centerline of a cylindrical microchannel was studied by direct numerical simulations.[99,106] Two particles in a Newtonian suspending fluid under inertialess conditions preserve their initial distance while traveling along the channel.[80] In contrast, fluid viscoelasticity leads to a variation of the interparticle

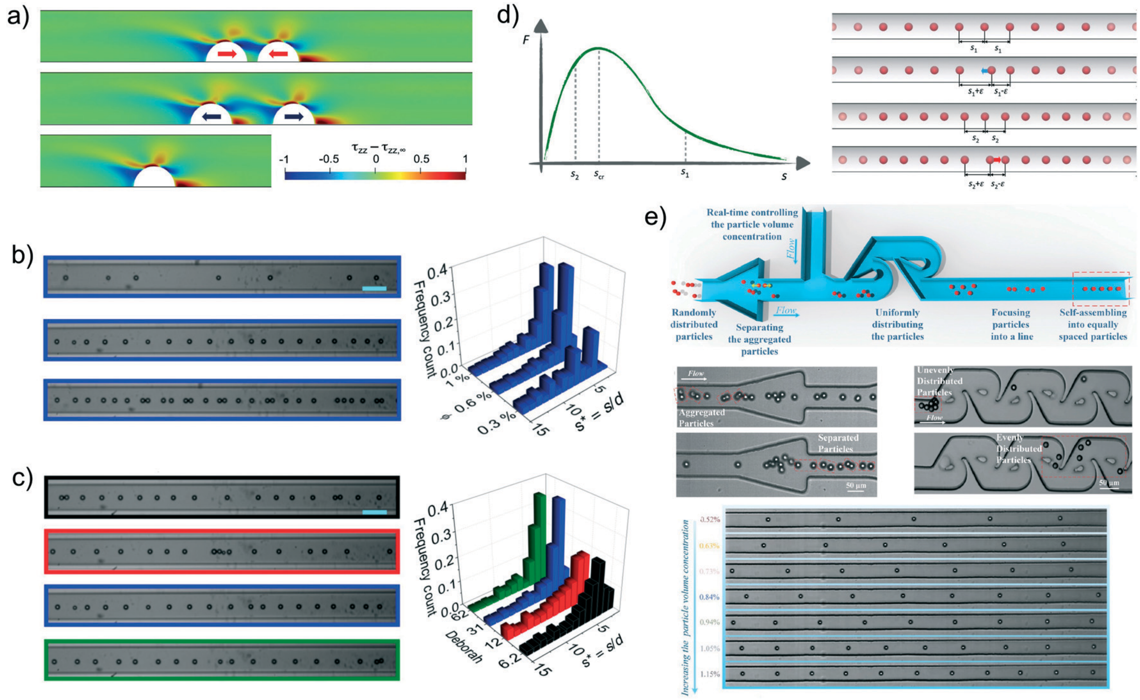

Fig. 8 a) Difference between the *zz*-component of the viscoelastic stress tensor and the same component of the unperturbed fluid for a particle pair (top and middle panel) or a single sphere (bottom panel) in a viscoelastic fluid modelled with the Giesekus constitutive equation. The Deborah number is De = 1, the confinement ratio is $\beta = 0.4$, and the Giesekus mobility parameter is $\alpha = 0.2$. The pairs in the top and middle panels have an initial center-to-center distance of 1.25 and 2 particle diameters, respectively. Adapted by permission from Springer Nature: *Microfluidics and Nanofluidics*: Numerical simulations on the dynamics of a particle pair in a viscoelastic fluid in a microchannel: effect of rheology, particle shape, and confinement, D'Avino *et al.*,[99] Copyright 2019. b) and c) Visualization of particle microstructure and interparticle distance distributions for a suspension of polystyrene particles in a shear-thinning solution of 1% wt hyaluronic acid in PBS at De = 31 and different volume fractions (b) and at $\phi = 0.6\%$ and different Deborah numbers (c). Reproduced from Del Giudice *et al.*,[100] Copyright 2018, American Physical Society. d) (Left) Sketch of the repulsive force between two particles in a viscoelastic fluid for a sufficiently high Deborah number. (Right) Schematic representation of the stability analysis of a particle train: a train of equally spaced particles at a distance $s_1 > s_{cr}$ is considered (first panel). A particle of the train is displaced by a small amount ε and experiences two different repulsive forces from the trailing and the leading sphere. Since s_1 is in the branch where the force F has a negative slope, the force between the displaced particle and the leading one is lower than the force between the particle and the trailing sphere. The net force is, then, toward the trailing sphere (blue arrow) and the interparticle distances are restored to the original value s_1 (second panel). The same scenario is considered with an equilibrium distance $s_2 < s_{cr}$ (third panel). After displacing the particle, the force between the displaced sphere and the leading one is higher than the force between the particle and the trailing sphere. Thus, the displaced sphere moves toward the leading one and a pair is formed (fourth panel). Reprinted with permission from Del Giudice *et al.*,[100] *Physical Review Applied*, **10**, 064058, 2018 Copyright (2018) by the American Physical Society. e) Schematic illustration of the microfluidic channel based on an array of swirl mixing channels. Snapshots of the particle arrangements in the array of inverted triangular microchannels, in an array of swirl mixing channels, and in the final straight microchannel (at different particle concentrations) are shown. Reprinted from ref. 101 with permission from the Royal Society of Chemistry.

distance depending on the Deborah number and the initial distance. For a Deborah number lower than a threshold $\mathrm{De}_{\mathrm{cr}}$, two scenarios are possible depending on the initial interparticle distance. For a pair of particles closer than a critical distance s_{cr}, the leading sphere travels at a velocity lower than the trailing one and the interparticle distance progressively reduces until forming a doublet. On the contrary, for an initial distance higher than s_{cr}, the leading sphere travels faster than the trailing one and the two particles move away until reaching a sufficiently large distance such that hydrodynamic interactions become negligible. The critical distance s_{cr} can be then regarded as an unstable equilibrium point. As the Deborah number increases, the critical distance progressively reduces and the region leading to doublet formation becomes narrower. For a Deborah number higher than the threshold $\mathrm{De}_{\mathrm{cr}}$, the interparticle distance increases regardless of the initial distance. Fluid shear-thinning and high confinement ratio values move the critical Deborah number $\mathrm{De}_{\mathrm{cr}}$ to lower values, thus reducing the formation of doublets. The existence of an unstable equilibrium point at relatively small Deborah numbers has been related to the axial viscoelastic normal stress distribution around the two particles.[99] In the top and middle panels of Fig. 8a the perturbation of the axial component of the viscoelastic stress due to the presence of the particles is shown for two particles at a distance lower and higher than s_{cr}. In the bottom panel of Fig. 8a the same quantity is reported for a single sphere. While the stress distribution around the external regions of each particle is unaffected by the presence of the other particle (compare with the single particle case), the local stress in the gap of the pair is strongly influenced by the distance. As the two particles are sufficiently close (top panel of Fig. 8a), the fluid in the gap moves at approximately the same velocity of the pair resulting in a small velocity gradient that, in turn, produces low viscoelastic stresses. Hence, the external normal forces prevail and push the particles close to each other. At a larger distance (middle panel of Fig. 8a), high stress regions appear in the fluid within the gap that counteract the external forces. The effect of the axial viscoelastic stress component on the pair dynamics was further confirmed by analyzing the case of two spheroidal particles.[99] For high aspect ratios, the two spheroids repel regardless of the Deborah number and the initial distance. The distribution of the viscoelastic stress in the gap shows the existence of high stress regions due to the large curvature near the tip of the spheroids even at very small interparticle distances.

The case of three aligned particles showed a richer behavior[106] as the dynamics depends on two relative distances. For a Newtonian inertialess fluid, the long-time configuration consists in a pair made of the trailing and middle sphere whereas the leading one moves far away until becoming isolated.[80,106] The distance of the particles forming the pair achieves a constant value depending on the two initial relative distances. In a viscoelastic fluid, the triplet dynamics is more complex and, as for the pair, the Deborah number is the most relevant parameter in order to identify possible scenarios. For values lower than a threshold $\mathrm{De}_{\mathrm{cr}}$, the triplet dynamics is determined by the two relative distances. For an initial configuration such that at least one of these two distances is below a critical value, the leading and middle sphere reduce their distance, whereas the leading one moves away. The long-time configuration is then made of a doublet (trailing and middle particles) and an isolated sphere (leading particle). In contrast, for initial distances higher than a critical value, both relative distances increase in time leading to the formation of three isolated particles. The latter is the only possible scenario for a Deborah number higher than $\mathrm{De}_{\mathrm{cr}}$.

The theoretical analysis of the dynamics of pairs and triplets of particles aligned at the centerline of a microchannel and immersed in a viscoelastic liquid showed the existence of an unstable critical distance. Consequently, two particles can reduce their distance while traveling along the channel forming a doublet or move far away until becoming isolated. The latter scenario is favored at high Deborah numbers and for strongly shear-thinning fluids. In a system made of several aligned particles at a sufficiently high volume fraction, each particle is surrounded by a trailing and leading particle. Let us assume that two particles of the train are at a distance higher than the critical one so that they move away. At some point both particles will 'feel' the presence of the surrounding particles, preventing the formation of isolated particles. As one particle starts to hydrodynamically interact with the next (or the previous) one, viscoelasticity immediately prevents them to approach as the distance between the new pair is of course higher than the critical one. A balance of these 'repulsive forces' suggests the possibility to generate a microstructure made of equally-spaced particles.

4.2.2 Particle trains. The first experimental evidence of self-assembly of particle trains driven by viscoelasticity was reported for a suspension of polystyrene particles at a volume fraction from 0.3 wt% to 1 wt% in a shear-thinning solution of 1 wt% hyaluronic acid in PBS.[100] At the lowest volume fraction, a clear ordering was not observed as the interparticle distances were too large, resulting in weak hydrodynamic interactions (Fig. 8b). On the contrary, at the highest volume fraction, the particles were very close one to each other and several doublets were visible. The optimal situation was found for the intermediate volume fraction where a preferential distance could be observed at high values of the Deborah number. Interestingly, this equilibrium distance was independent of the Deborah number (Fig. 8c). No ordering was instead found for a 0.1% wt hyaluronic acid in PBS characterized by a constant viscosity.[100] Similar results were obtained very recently by Jeyasountharan *et al.*,[107] who employed an aqueous 0.1 wt% xanthan gum solution as suspending liquid, and demonstrated viscoelastic ordering of particles on the centreline of a serpentine microchannel.

Numerical simulations have been also carried out to understand the train dynamics.[100,108] To follow the motion of a large number of particles, the simulations assumed that each particle of the train hydrodynamically interacted with the previous and the next one, ignoring the presence of the other particles. Hence, the train could be decomposed in several systems made of three particles for which the relative velocities needed to update the relative distances were computed through direct numerical simulations.[106] The simulation results confirmed the experimental evidences, reporting no relevant ordering at low volume fractions, a preferential distance at higher volume fractions, and a more and more frequents of doublets as the volume fraction is further increased. An interesting outcome of the simulations was the formation of doublets even at a Deborah number higher than the critical value $\mathrm{De}_{\mathrm{cr}}$ where two or three spheres repelled regardless of their relative distances. A qualitative argument based on a stability analysis was proposed to justify this behavior.[100] With reference to Fig. 8d, a train of equally-spaced particles at some distance s_1 is considered. In the left panel of Fig. 8d, a schematic of the interparticle force between a pair as a function of the relative distance is sketched for $\mathrm{De} > \mathrm{De}_{\mathrm{cr}}$ based on direct simulation results.[106] The force is positive for any distance denoting that the two particles separate. Let us also assume that the equilibrium distance of the train is larger than the critical distance corresponding to the maximum in Fig. 8d. If one particle of the train was displaced approaching the leading one, the relative distance between these two particles reduce, corresponding to an increase of the repulsive force. Similarly, as the displaced particle moves far away from the trailing one, the distance increases corresponding in a lower force. As a result, the net force acting on the displaced particle is opposite to the direction of the displacement and the original train is restored. On the contrary, for a train characterized by an equilibrium distance lower than the maximum, a displaced particle feels a force directed towards the direction of the displacement, forming a doublet (bottom panel of Fig. 8d).

Experiments and simulations also highlighted the importance of the initial distribution of the interparticle distances. Indeed, once aligned at the centerline, particles that ended up very close one to each other were hardly separated while traveling through the channel,[100,101,108] obviously reducing the ordering efficiency. The microfluidic device must be properly designed in order to prevent the injection of agglomerates of particles from the reservoir or to separate the aligned particles before ordering takes place. The latter was accomplished by designing a channel with an array of swirl mixing channels[101] shown in Fig. 8e. The overall device was made of a sequence of inverted triangular microchannels and straight microchannels aimed at separating the particles. The suspension then passed through the array of swirl mixing channels, leading to a spatial uniform distribution of the flowing particles. Finally, the suspension reached a straight channel where first focusing and then ordering took place. A lateral channel where the suspending fluid was injected was placed between the two sets of geometrical elements in order to adjust the volume fraction. The results showed the formation of highly equally-spaced structures for particle volume concentration from 0.5% to 1.15% (bottom panel of Fig. 8e).

The aforementioned studies clearly showed the capability of viscoelastic fluids to self-assemble particles in equally-spaced aligned structures. A relevant aspect of using elastic effects was that focusing and then ordering took place in the same microchannel. At variance with inertial ordering, the formation of a train was along the channel centerline with several advantages for a variety of microfluidic applications. For instance, at the channel centerline the shear stresses experienced by the particles are minimal, allowing the processing of soft cells. Also, the rotation rate of the aligned particles/cells is small (in theory nil for a perfect alignment) avoiding blurred images in cytometry applications that employ line-scan based interrogation.

Several aspects, however, need to be further investigated. The formation of doublets or, more in general, of strings of particles in contact, is a critical issue. The presence of strings is due to the direction of the viscoelastic normal forces acting between two aligned particles. Crucial is the initial distribution of the particle distances and, in particular, the presence of close particles after the focusing mechanism. Even when the elastic forces between adjacent particles tend to separate them regardless the relative distance, string formation is still observed. A properly design of the feeding process aimed at avoiding the formation of agglomerates of particles is required. An important parameter affecting the probability of string formation is the particle volume concentration. A relatively large value promotes particle pairing with a detrimental effect on the ordering efficiency. On the other side, a low value of particle volume concentration may result in large average interparticle distances and weak hydrodynamic interactions so that the train microstructure does not change. Hence, viscoelastic ordering properly works in a window of solid volume concentration. In fact, rather than the nominal particle volume concentration, a more relevant quantity to be considered to assess the quality of the ordering is the local volume concentration, *i.e.*, the concentration of particles along the train. Such a quantity may strongly vary during an experiment due to disturbances of the applied flow rate or pressure drop, or to the presence of an agglomerate of particles in the reservoir. These disturbances may lead to zones of the train with or without several particles, reducing in both cases the ordering efficiency.

The re-arrangement of the microstructure hopefully leading to an equally-spaced train is due to a difference of the translational velocity of the flowing particles, resulting in a continuous variation of their mutual distances. The relative velocity between consecutive particles is 3–4 orders of magnitude lower than their translational velocity. Hence, microchannels with a length much larger than the characteristic size of the cross-section are required to obtain an appreciable modification of the interparticle distance distribution. For instance, in a straight microchannel with length one thousand times higher than the side of the cross-section the distance distribution is still evolving as the train reaches the end of the channel.[100,108] Curved or spiraling microchannels could help in extending the total length while keeping the overall chip surface small. In this case, the effect of a curvature of the streamlines of the flow field on the ordering dynamics should be investigated. Another possibility could be the periodical inversion of the flow field in a straight channel to mimic an infinite length as adopted for inertial ordering[90] or for enhancing the viscoelastic focusing.[109] An inversion of the flow, however, leads to a transient redistribution of the viscoelastic stresses between the particles, likely affecting the ordering mechanism.

The physical mechanism behind the dynamics of the pair is quite well-understood and the effect of the relevant parameters (rheology, flow rate, confinement ratio) has been thoroughly investigated. A similar in-depth theoretical analysis for the triplet dynamics is not available and only a couple of Deborah numbers have been analyzed. Since the train dynamics is determined by the interaction of each particle with at least the trailing and leading one, a more detailed study on the three-particle system is required. Similarly, the experimental and numerical studies on the train dynamics are limited to a couple of suspending fluids and to a fixed value of the confinement ratio. Regarding the fluid rheology, experiments have evidenced that ordering is possible in a shear-thinning fluid, while a sequence of particle strings are observed in an elastic fluid characterized by a constant viscosity. Although this is partially confirmed by the theoretical analysis on the pair dynamics, a clear explanation is missing. Similarly, the effect of the confinement ratio on the train dynamics is not yet explored. A useful information comes from the pair dynamics where lowering the confinement ratio results in a significant reduction of the relative velocity. This is expected as the hydrodynamic interactions between smaller particles are weaker. Furthermore, a lower confinement ratio also leads to an extension of the attractive region between the particles of the pair at higher Deborah numbers. On the basis of these results, a suspension of smaller particles would require much longer channels to re-arrange the microstructure and the formation of strings is favored.

Finally, it has to be mentioned that the available results have investigated the possibility to achieve ordering by exploiting purely viscoelastic effects. The flow and fluid conditions, indeed, are such that the Reynolds number is much less than unity, ruling out inertial effects. Motivated by the successful combination of inertia and viscoelasticity to enhance particle focusing,[76,78] the 'inertio-elastic ordering' might have interesting potentialities. For instance, inertial effects, that generally produce opposite results with respect to elastic ones, could reduce (or even revert) the direction of the repulsive interparticle forces and promote the formation of more stable trains. This possibility definitely merits further investigation.

5 Microfluidic crystals and compartmentalisation

Formation of droplet and particle crystals can be seen as the 'prelude' to a vast range of applications featuring both types of crystals. On the one hand, microfluidic crystals can be used to enhance the compartmentalisation efficiency of particles and cells in order to defeat the Poisson statistic problem, which is a very important aspect when targeting single-cell analysis.[93,110–113] On the other hand, compartmentalisation of either rigid particles or liquid droplets in another larger droplet where they can self-assemble in ordered crystals (similarly to the work by Postek *et al.*[48]) is appealing for the fabrication of colloidal crystals[114,115] and photonic materials.[116] In this section, we review some of the most recent advances in microfluidic crystals and compartmentalisation, citing also some pioneering works in the field. A broader overview of the applications related to microfluidic compartmentalisation (not only crystals) can be found in the following recent reviews: encapsulation,[117] single-cell analysis,[118] multiple emulsions,[119,120] self-assembly,[121] and production of biomaterials.[122]

5.1 Deterministic encapsulation

Deterministic encapsulation (or compartmentalisation) is a procedure where a constant pre-defined number of objects (particles or cells) are encapsulated in each single droplet without empty droplets nor a different number of objects per droplet. The deterministic encapsulation can take place when the frequency of droplet formation is proportional to the frequency of the objects reaching the encapsulation area. For instance, to encapsulate one particle in one droplet, the frequency of the particle crystal approaching the encapsulation area should be equal to the droplet crystal formation frequency. A purely hydrodynamic deterministic encapsulation can then take place when droplet crystals 'meet' particle crystals at the encapsulation area. Edd *et al.*[93] were among the firsts to introduce this concept and demonstrated that inertially-formed particle trains flowing on two equilibrium lines (2D particle crystal) coupled to a flow focusing droplet geometry for the generation of 1D droplet crystals led to the controlled encapsulation of particles in droplets with an efficiency of over 80%. This approach has been perfected later by Kemna *et al.*[110] that employed a spiral microfluidic channel to form 1D particle crystals by reducing the focusing equilibrium position of the particles from two (as in Edd *et al.*[93]) to one. Other ways to increase the encapsulation efficiency such as complex geometries,[112] and multi-droplet merging[113] have been also introduced. However, these studies mainly focused on the encapsulation of a single object, whereas in applications such as drop-sequencing,[125] where barcoded beads are encapsulated together with cells for single-cell analysis, it is important to encapsulate two objects simultaneously (*e.g.*, one particle and one cell). Lagus and Edd[111] employed a microfluidic device where two sets of particles or cells were encapsulated simultaneously in a single droplet with an efficiency of 65%, 5-folds larger than the one dictated by the Poisson statistic. We now highlight two recent works that successfully employed 1D particle and cell train crystals for single-cell analysis using Drop-seq techniques. Moon *et al.*[126] used a spiral microfluidic channel to obtain inertial-driven 1D

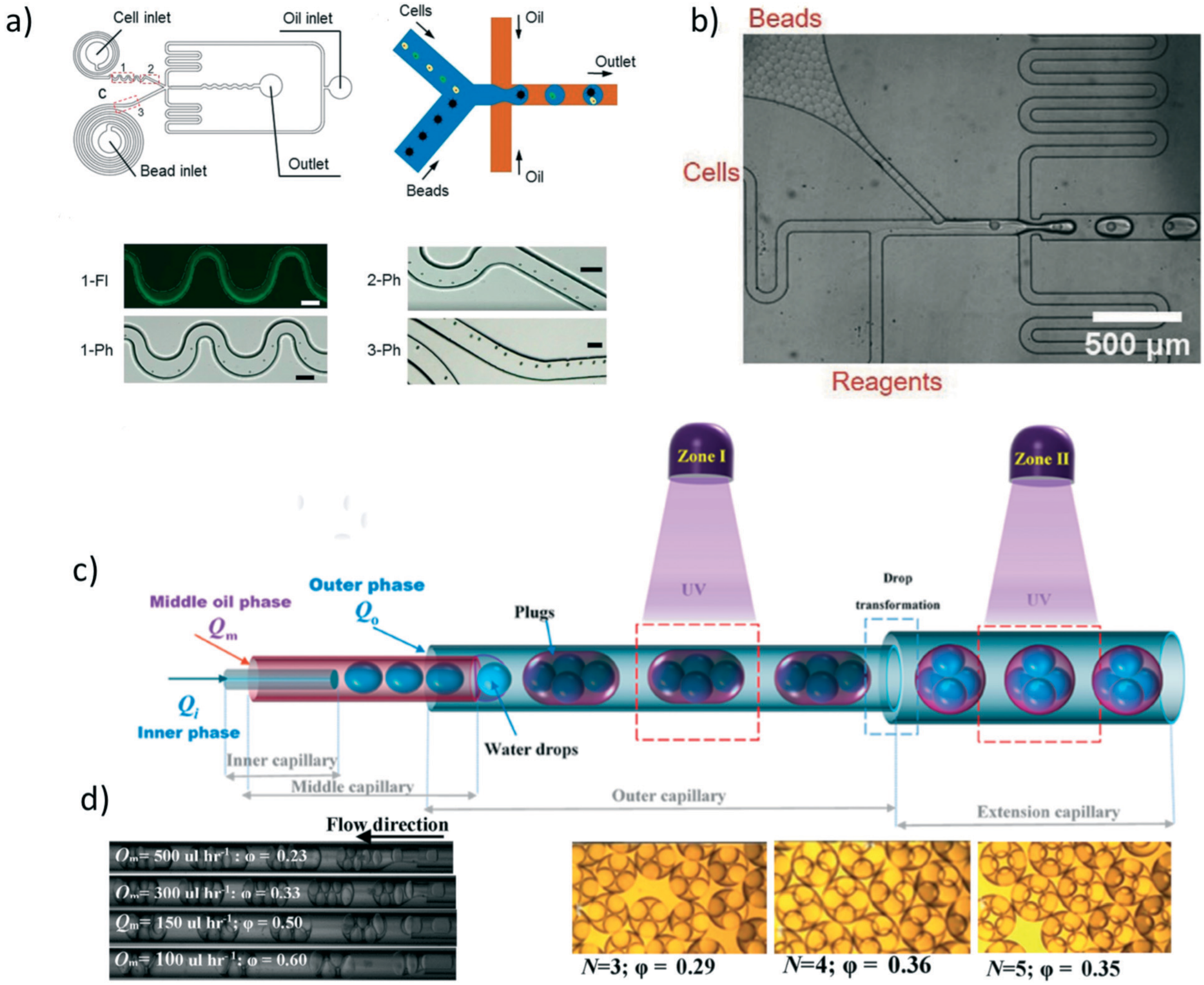

Fig. 9 a) Dean-flow assisted 1D cell and particle inertial crystal formation for Drop-seq analysis. Schematic of the device and experimental snapshots are also reported. Reprinted with permission from Li *et al.*,[123] Dean flow assisted single cell and bead encapsulation for high performance single cell expression profiling, *ACS Sensors*, **4**, 1299, Copyright 2019, American Chemical Society. b) Microfluidic device employed to deterministically dissolve polyacrylamide barcoded beads in droplets containing cells. Reprinted from Wang *et al.*,[124] Dissolvable polyacrylamide beads for high-throughput droplet DNA barcoding, *Advanced Science*, **7**(8), 1903463, 2020. c) 'On the fly' fabrication of porous microparticles using double emulsions. Droplets self-assemble in crystals within another larger droplet and are photopolymerised. d) Experimental snapshots of double emulsions in different flow conditions (left) and self-assembled structures (right). Panels c) and d) are reprinted with permission from Sajjadi *et al.*,[115] 'On-the-fly' fabrication of highly-ordered interconnected cylindrical and spherical porous microparticles *via* dual polymerization zone microfluidics, *Langmuir*, **35**, 12731, Copyright 2019, American Chemical Society.

particle crystals; the spiral channel was coupled to a flow-focusing geometry where flowing cells were then encapsulated together with the barcoded particles with an efficiency of roughly 98%. In this way, the authors performed single-cell RNA extraction from HEK293 and IH3T3 mouse cell lines. Despite a substantial efficiency improvement, a step further was introduced by Li *et al.*[123] that employed two independent spiral channels to self-order both particles and cells prior to the encapsulation area (Fig. 9a). By synchronising the frequency of particle and cell arrival with that of droplet formation, they obtained up to 300% increase in cell-utilisation rate compared to conventional Drop-seq techniques. To the best of our knowledge, the two works above are the only ones that employed inertial ordering finalised to Drop-seq analysis. Follow-up works will need to achieve truly deterministic encapsulation, meaning an efficiency of 100%, which would lead to the identification of rare cells such as circulating tumour cells. Moreover, the formation of particle crystals in viscoelastic solutions is an entirely new field that is awaiting further developments. We are currently not aware of any work featuring the encapsulation of particles or cells in polymer solutions: we ascribe this to the fact that droplets made of polymer solutions are difficult to form because of the elastic stresses that delay the droplet formation at the microfluidic junction.[127] An interesting variation to the encapsulation strategies presented above has been introduced by Clark and Abate[128] where droplet formation was 'triggered' by the beads and the cells during their flow. The authors successfully achieved bead-cell encapsulation at a rate of 20 kHz. We expect that this method can be optimised to account for different cell lines as well as different cell types. It also offers a promising route to achieve Drop-seq technologies in a centrifugal microfluidic device, as the continuous phase could be pre-loaded, while the dispersed phase containing the particles could then trigger the encapsulation. This is particularly challenging because, to our knowledge, there are no works featuring train formation in centrifugal microfluidic devices: addressing this issue can open new opportunities for centrifugal microfluidics.

Another technique to encapsulate cells together with particles was introduced by Abate *et al.*[129] Instead of using rigid particles that can clog the channel at large concentrations, the authors employed deformable microgels that were self-assembled to form a 2D droplet crystal in a near-tapered geometry (similarly to Gai *et al.*[21]). The 2D crystal was then forced to flow in a channel with size equal to that of a single microgel while two lateral channels pumping water contributed to equally-space the microgels in a 1D microgel crystal. Finally, the microgels in the 1D crystal were encapsulated using downstream flow-focusing droplet formation, with 98% efficiency. This approach, however, could not be used for Drop-seq applications as there was the need of introducing easy to fabricate deformable barcoded particles (in contrast with the most common rigid ones). Very recently, this problem has been addressed by Wang *et al.*[124] that reported continuous microfluidic fabrication of dissolvable barcoded polyacrylamide beads. They employed a device where the dissolvable beads were arranged in a 2D crystal using a nearly tapered device (Fig. 9b). The authors employed the beads for single cell RNA protein analysis. Considering that the production of soft barcoded beads has been presented only recently and that cells were not ordered in the work by Wang *et al.*,[124] we soon expect new works featuring the deterministic Drop-seq of cells using dissolvable barcoded beads.

5.2 Crystal formation in droplets

The possibility of forming crystal-like structures within droplets in microfluidic devices has been introduced by Yi *et al.*[130] The authors first encapsulated microspheres using the same device of Thorsen *et al.*;[11] while moving downstream, the water layer of the droplet surrounding the microspheres was slowly absorbed by the oil (continuous phase) causing droplet shrinkage and self-assembly of the particles in the droplet. Similar approaches have been also explored for the formation of colloidosomes,[131] celloidosomes,[132] photonic materials[116] and three-tier hierarchical assemblies.[133] However, with the exception of the work by Yi *et al.*,[130] these approaches required a step external to the microfluidic device in order to facilitate the droplet evaporation with consequent self-assembly of the compartmentalised particles. Controlled self-assembly of several structures containing chemically functionalised particles has instead been introduced by Xu *et al.*[114] In their work, the authors were able to fabricate droplet crystals having different structures based on the combination of chemical particle properties and self-assembly internal to the droplets. The final configuration of the crystal was expected to depend upon the chemical composition of the particles, thus requiring future works in order to clarify how chemical properties of the particles affect the crystal formation.

A more controlled approach for the fabrication of compartmentalised crystal structures is based on doublet emulsions, *i.e.*, a multiple-phase dispersion in which droplets enclosing fined droplets are suspended in a continuous liquid phase[134,135] (the interested reader is referred to the recent review by Sattari *et al.*[119]). An interesting development has been presented by Sajjadi *et al.*[115] who introduced a microfluidic device for the formation of double emulsions based on the co-flow droplet generation geometry. With reference to Fig. 9c, the double emulsions were formed first; then, the shape of their external droplet changed according to the diameter of the two series of capillaries. Two photopolymerisation zones were added to then polymerise the assembled structures. The advantage of this approach over others was the fact that the large droplet relaxed in a more spherical configuration when the double emulsion reached the last microchannel: consequently, the internal droplets self-assembled within the larger droplet in crystals that were thermodynamically favoured, thus making the whole process pseudo-deterministic, with very well defined crystal-like structures (left snapshots in Fig. 9d). After polymerisation, the external layer of the large droplet ruptured, resulting in the formation of hollow particles. We expect this approach to be useful also for the fabrication of plasmonic materials as previously suggested by Morozov and Leshansky.[70] A similar technique can be coupled to that by Shen *et al.*[66] to obtain a rich portfolio of colloidal structures having different properties. Recent advances in the understanding of the fluid dynamics of the fluid inside the double emulsions[136,137] is also expected to simplify the fabrication of colloidal structures.

6 Conclusions and perspectives

The advent of microfluidics contributed to introduce a vast range of tools to control the position of objects down to the sub-micrometer scale, thus enabling the generation of crystal-like structures in confined flows. A significant amount of literature has been published on microfluidic crystals. Some of these works highlight the physical mechanisms behind the self-assembly of droplets/particles mediated by hydrodynamic interactions, the stability of the microstructure, and the effect of the relevant parameters. Other works focus on the engineerization of the crystal-like structures introducing new droplet-based technologies for single-cell analysis or colloidal synthesis, devices for deterministic encapsulation, *etc.* The physical mechanism governing the collective motion of droplets is of different nature as compared to that involved in self-assembly of particles induced by inertia or viscoelasticity. In the former case, the inter-droplets forces are generated by the disturbance of the flow field induced by the droplet motion coupled with confinement effects, resulting in a dipole–dipole interaction. Inertial ordering of particles is, instead, driven by inertial forces that push the particles to equilibrium positions and repulsive viscous forces that stabilize the microstructure setting the inter-particle spacing. Elastic forces, originated by the orientation and stretching of polymer chains under flow, rule viscoelastic ordering. These forces lead to the alignment of particles along the channel centreline and modulate the inter-particle spacing. The different underlying self-assembly mechanisms reflect on different stability properties of the formed crystals as well as on the dimensionality of the resulting structures. Droplets can arrange in 1D, 2D, and 3D structures depending on the microchannel geometry. 1D equally-spaced structures can be easily generated with a well-controlled spacing. However, their stability requires strong confinements in two directions. In unconfined geometries, transversal local fluctuations of the droplet crystal may grow, leading to crystal instability. In contrast, 1D structures of particles are more stable as a transversally displaced particle is restored to its equilibrium position along the train by an inertial or viscoelastic lateral force component. Since particles are not formed but are randomly injected in the microchannel, the control of the inter-particle spacing is not straightforward. Research is active in this direction to understand the conditions leading to equally-spaced structures in inertial and viscoelastic ordering, required to design efficient particle-in-droplet encapsulation devices.

Despite the different mechanisms involved in droplet and particle crystal formation, the underlying physics have several common features. First, all the governing forces are of hydrodynamic nature, leading to the formation of the microstructure without the need of external forces. Furthermore, the formation and evolution of both droplet and particle crystals is strongly affected by confinement effects, making microfluidics the natural framework to work with. Finally, the phonon-like behaviour in 1D structures has been observed in droplet crystals, inertial and viscoelastic ordering. We believe that there is a need to tackle the phenomenon of microfluidic crystal formation under a more holistic point of view, where a detailed understanding of the hydrodynamic interactions among different objects (*i.e.*, particles, cells, droplets) can lead to a generalised framework to design *a priori* microfluidic devices for targeted applications.

There is room for developing new technologies that are currently missing. The recent fabrication of barcoded dissolvable beads[124] together with the principles of deterministic encapsulation[129] may open a new generation of optimised Drop-seq technologies. The experimental evidence of particle ordering on the centreline of a straight microchannel when the suspending liquid is viscoelastic and shear-thinning is expected to drive new research.

Continuous generation of viscoelastic droplets will also close the gap with inertial microfluidics, enabling further studies on viscoelastic Drop-seq technologies. The capability of self-order different kinds of particles and encapsulate them in a multi-droplet system would generate an isolated environment where complex reactions, mass transfer, biological activity, controlled drug release, *etc.* could take place. Similarly, recent advances in colloidal crystal fabrication can prompt new directions in material science for the production of photonic materials, provide new tools for drug delivery applications, generate complex structures from simple building blocks, combine objects with different physical or chemical properties to create a material with unique characteristics. Very recently, an interest in the self-assembly of 'active' droplets and particles arose,[138–140] with potential advancements in the field yet to be explored.

Finally, the advent of machine learning and artificial intelligence can provide a significant boost to the field (see the recent review by Isozaki *et al.*[141]). The complexity of solving a multi-body problem associated to crystal formation could be tackled by using machine learning techniques with predictive outcomes, thus leading to a AI-aided technology for crystal design. Similarly, deterministic encapsulation could be triggered by artificial intelligence consequently to object recognition.[142,143] The capacity of elaborating large amount of data together with intrinsic predictive functionalities, makes artificial intelligence among the most suitable candidates to face the challenges associated to the derivation of a general framework for the production of microfluidic crystals.

Conflicts of interest

There are no conflicts to declare.

Acknowledgements

FDG acknowledges support from EPSRC New Investigator Award (Grant Ref. No. EP/S036490/1).

References

1 A. Stevenson, *Oxford dictionary of English*, Oxford University Press, USA, 2010.

2 T. M. Squires and S. R. Quake, *Rev. Mod. Phys.*, 2005, **77**, 977.

3 J. Nunes, S. Tsai, L. D. Landau, E. M. Lifshitz, J. Wan and H. A. Stone, *J. Phys. D: Appl. Phys.*, 2013, **46**, 114002.

4 P. Zhu and L. Wang, *Lab Chip*, 2017, **17**, 34–75.

5 J. Guerrero, Y.-W. Chang, A. A. Fragkopoulos and A. Fernandez-Nieves, *Small*, 2020, **16**, 1904344.

6 T. Beatus, R. H. Bar-Ziv and T. Tlusty, *Phys. Rep.*, 2012, **516**, 103–145.

7 T. Beatus, I. Shani, R. H. Bar-Ziv and T. Tlusty, *Chem. Soc. Rev.*, 2017, **46**, 5620–5646.

8 T. Beatus, T. Tlusty and R. Bar-Ziv, *Nat. Phys.*, 2006, **2**, 743–748.

9 T. Beatus, R. Bar-Ziv and T. Tlusty, *Phys. Rev. Lett.*, 2007, **99**, 124502.

10 J.-B. Fleury, U. D. Schiller, S. Thutupalli, G. Gompper and R. Seemann, *New J. Phys.*, 2014, **16**, 063029.

11 T. Thorsen, R. W. Roberts, F. H. Arnold and S. R. Quake, *Phys. Rev. Lett.*, 2001, **86**, 4163.

12 L. D. Landau and E. M. Lifshitz, Fluid Mechanics, Pergamon Press, 1987.

13 B. Liu, J. Goree and Y. Feng, *Phys. Rev. E: Stat., Nonlinear, Soft Matter Phys.*, 2012, **86**, 046309.

14 I. Sarig, Y. Starosvetsky and A. D. Gat, *J. Fluid Mech.*, 2016, **800**, 264–277.

15 Y. Green, *J. Fluid Mech.*, 2018, **853**, 253–270.

16 L. Wang and J. Wang, *Nanoscale*, 2019, **11**, 16708–16722.

17 A. C. Hatch, J. S. Fisher, A. R. Tovar, A. T. Hsieh, R. Lin, S. L. Pentoney, D. L. Yang and A. P. Lee, *Lab Chip*, 2011, **11**, 3838–3845.

18 V. Chokkalingam, S. Herminghaus and R. Seemann, *Appl. Phys. Lett.*, 2008, **93**, 254101.

19 U. D. Schiller, J.-B. Fleury, R. Seemann and G. Gompper, *Soft Matter*, 2015, **11**, 5850–5861.

20 S. Thutupalli, J.-B. Fleury, U. D. Schiller, G. Gompper, S. Herminghaus and R. Seemann, in *Engineering of Chemical Complexity II*, World Sci., Singapore, 2014, vol. 12, p. 125.

21 Y. Gai, C. M. Leong, W. Cai and S. K. Tang, *Proc. Natl. Acad. Sci. U. S. A.*, 2016, **113**, 12082–12087.

22 W. T. Read and W. Shockley, *Phys. Rev.*, 1950, **78**, 275.

23 Y. Gai, A. Bick and S. K. Tang, *Phys. Rev. Fluids*, 2019, **4**, 014201.

24 B. M. Jose and T. Cubaud, *Microfluid. Nanofluid.*, 2012, **12**, 687–696.

25 M. D. Raj and R. Rengaswamy, *Microfluid. Nanofluid.*, 2014, **17**, 527–537.

26 S. Yang, S. W. Ahn, A. R. Kang, D. Lee, S. S. Lee, J. M. Kim, K. H. Ahn and S. J. Lee, *Korea Aust. Rheol. J.*, 2011, **23**, 119.

27 M. Seo, Z. Nie, S. Xu, P. C. Lewis and E. Kumacheva, *Langmuir*, 2005, **21**, 4773–4775.

28 B. Shen, M. Leman, M. Reyssat and P. Tabeling, *Exp. Fluids*, 2014, **55**, 1728.

29 T. Ohmura, M. Ichikawa, K.-i. Kamei and Y. T. Maeda, *Appl. Phys. Lett.*, 2015, **107**, 074102.

30 E. Kadivar, *Phys. A*, 2016, **443**, 486–494.

31 E. Kadivar, M. Farrokhbin and F. Ghasemipour, *Braz. J. Phys.*, 2019, **49**, 140–150.

32 R. Mehrotra, N. Jing and J. Kameoka, *Appl. Phys. Lett.*, 2008, **92**, 213109.

33 A. C. Hatch, J. S. Fisher, S. L. Pentoney, D. L. Yang and A. P. Lee, *Lab Chip*, 2011, **11**, 2509–2517.

34 C. Priest, S. Herminghaus and R. Seemann, *Appl. Phys. Lett.*, 2006, **88**, 024106.

35 P. Parthiban, P. S. Doyle and M. Hashimoto, *Soft Matter*, 2019, **15**, 4244–4254.

36 M. Seo, Z. Nie, S. Xu, M. Mok, P. C. Lewis, R. Graham and E. Kumacheva, *Langmuir*, 2005, **21**, 11614–11622.

37 S. Fujiwara, K. Shoji, C. Watanabe, R. Kawano and M. Yanagisawa, *Micromachines*, 2020, **11**, 701.

38 J.-P. Raven and P. Marmottant, *Phys. Rev. Lett.*, 2009, **102**, 084501.

39 A. Montessori, M. Lauricella, A. Tiribocchi and S. Succi, *Phys. Rev. Fluids*, 2019, **4**, 072201.

40 J. Wang, M. Jin, T. He, G. Zhou and L. Shui, *Micromachines*, 2015, **6**, 1331–1345.

41 K. E. Sung, S. A. Vanapalli, D. Mukhija, H. A. McKay, J. Mirecki Millunchick, M. A. Burns and M. J. Solomon, *J. Am. Chem. Soc.*, 2008, **130**, 1335–1340.

42 D. Dendukuri and P. S. Doyle, *Adv. Mater.*, 2009, **21**, 4071–4086.

43 M. Hashimoto, P. Garstecki and G. M. Whitesides, *Small*, 2007, **3**, 1792–1802.

44 M. D. Raj and R. Rengaswamy, *Ind. Eng. Chem. Res.*, 2015, **54**, 10835–10842.

45 C. M. O'Keefe, A. M. Kaushik and T.-H. Wang, *Anal. Chem.*, 2019, **91**, 11275–11282.

46 Y. He, J. Yin, W. Wu, H. Liang, F. Zhu, Y. Mu, H. Fan and T. Zhang, *Anal. Chem.*, 2020, **92**, 8530–8535.

47 M. Nie, M. Zheng, C. Li, F. Shen, M. Liu, H. Luo, X. Song, Y. Lan, J.-Z. Pan and W. Du, *Anal. Chem.*, 2019, **91**, 1779–1784.

48 W. Postek, P. Gargulinski, O. Scheler, T. S. Kaminski and P. Garstecki, *Lab Chip*, 2018, **18**, 3668–3677.

49 X. Li, D. Zhang, W. Ruan, W. Liu, K. Yin, T. Tian, Y. Bi, Q. Ruan, Y. Zhao and Z. Zhu, *et al.*, *Anal. Chem.*, 2019, **91**, 13611–13619.

50 C. D. Ahrberg, A. Manz and B. G. Chung, *Lab Chip*, 2016, **16**, 3866–3884.

51 K. R. Sreejith, C. H. Ooi, J. Jin, D. V. Dao and N.-T. Nguyen, *Lab Chip*, 2018, **18**, 3717–3732.

52 J. Yin, Y. Suo, Z. Zou, J. Sun, S. Zhang, B. Wang, Y. Xu, D. Darland, J. X. Zhao and Y. Mu, *Lab Chip*, 2019, **19**, 2769–2785.

53 D. Pekin, Y. Skhiri, J.-C. Baret, D. Le Corre, L. Mazutis, C. B. Salem, F. Millot, A. El Harrak, J. B. Hutchison and J. W. Larson, *et al.*, *Lab Chip*, 2011, **11**, 2156–2166.

54 V. R. Yelleswarapu, H.-H. Jeong, S. Yadavali and D. Issadore, *Lab Chip*, 2017, **17**, 1083–1094.

55 X. Bian, F. Jing, G. Li, X. Fan, C. Jia, H. Zhou, Q. Jin and J. Zhao, *Biosens. Bioelectron.*, 2015, **74**, 770–777.

56 S. Tian, Z. Zhang, J. Chen, M. Du, Z. Li, H. Yang, X. Ji and Z. He, *Talanta*, 2018, **186**, 24–28.

57 C.-Y. Ou, T. Vu, J. T. Grunwald, M. Toledano, J. Zimak, M. Toosky, B. Shen, J. A. Zell, E. Gratton and T. J. Abram, *et al.*, *Lab Chip*, 2019, **19**, 993–1005.

58 X. Xu, H. Yuan, R. Song, M. Yu, H. Y. Chung, Y. Hou, Y. Shang, H. Zhou and S. Yao, *Biomicrofluidics*, 2018, **12**, 014103.

59 W. Postek, T. Kaminski and P. Garstecki, *Lab Chip*, 2017, **17**, 1323–1331.

60 F. Schuler, F. Schwemmer, M. Trotter, S. Wadle, R. Zengerle, F. von Stetten and N. Paust, *Lab Chip*, 2015, **15**, 2759–2766.

61 F. Schuler, M. Trotter, M. Geltman, F. Schwemmer, S. Wadle, E. Domínguez-Garrido, M. López, C. Cervera-Acedo, P. Santibáñez and F. von Stetten, *et al.*, *Lab Chip*, 2016, **16**, 208–216.

62 H. Peng, M. Zhu, Z. Gao, C. Liao, C. Jia, H. Wang, H. Zhou and J. Zhao, *Biomed. Microdevices*, 2020, **22**, 1–10.
63 Y. Wang, S. Liu, T. Zhang, H. Cong, Y. Wei, J. Xu, Y.-P. Ho, S.-K. Kong and H.-P. Ho, *Lab Chip*, 2019, **19**, 3870–3879.
64 L. Clime, L. Malic, J. Daoud, L. Lukic, M. Geissler and T. Veres, *Lab Chip*, 2020, **20**, 3091–3095.
65 Y.-T. Kao, T. S. Kaminski, W. Postek, J. Guzowski, K. Makuch, A. Ruszczak, F. von Stetten, R. Zengerle and P. Garstecki, *Lab Chip*, 2020, **20**, 54–63.
66 B. Shen, J. Ricouvier, F. Malloggi and P. Tabeling, *Adv. Sci.*, 2016, **3**, 1600012.
67 M. D. Raj, A. Gnanasekaran and R. Rengaswamy, *Soft Matter*, 2019, **15**, 7863–7875.
68 F. Bian, L. Sun, L. Cai, Y. Wang, Y. Wang and Y. Zhao, *Small*, 2020, **16**, 1903931.
69 W. Li, H. Palis, R. Mérindol, J. Majimel, S. Ravaine and E. Duguet, *Chem. Soc. Rev.*, 2020, **49**, 1955–1976.
70 K. I. Morozov and A. M. Leshansky, *Langmuir*, 2019, **35**, 3987–3991.
71 Z. Ge, O. Tammisola and L. Brandt, *Soft Matter*, 2019, **15**, 3451–3460.
72 J. Zhou and I. Papautsky, *Lab Chip*, 2013, **13**, 1121–1132.
73 H. Amini, W. Lee and D. D. Carlo, *Lab Chip*, 2014, **14**, 2739–2761.
74 D. Stoecklein and D. Di Carlo, *Anal. Chem.*, 2018, **91**, 296–314.
75 G. D'Avino, F. Greco and P. L. Maffettone, *Annu. Rev. Fluid Mech.*, 2017, **49**, 341–360.
76 D. Yuan, Q. Zhao, S. Yan, S.-Y. Tang, G. Alici, J. Zhang and W. Li, *Lab Chip*, 2018, **18**, 551–567.
77 M. K. D. Manshadi, M. Mohammadi, L. K. Monfared and A. Sanati-Nezhad, *Biotechnol. Bioeng.*, 2019, **117**, 580–592.
78 J. Zhou and I. Papautsky, *Microsyst. Nanoeng.*, 2020, **6**, 113.
79 M. Baron, J. Bławzdziewicz and E. Wajnryb, *Phys. Rev. Lett.*, 2008, **100**, 174502.
80 P. J. A. Janssen, M. D. Baron, P. D. Anderson, J. Blawzdziewicz, M. Loewenberg and E. Wajnryb, *Soft Matter*, 2012, **8**, 7495.
81 K. J. Humphry, P. M. Kulkarni, D. A. Weitz, J. F. Morris and H. A. Stone, *Phys. Fluids*, 2010, **22**, 081703.
82 W. Lee, H. Amini, H. A. Stone and D. Di Carlo, *Proc. Natl. Acad. Sci. U. S. A.*, 2010, **107**, 22413–22418.
83 Z. Pan, R. Zhang, C. Yuan and H. Wu, *Phys. Fluids*, 2018, **30**, 102005.
84 C. Schaaf and H. Stark, *Eur. Phys. J. E: Soft Matter Biol. Phys.*, 2020, **43**, 50.
85 W. Tang, S. Zhu, D. Jiang, L. Zhu, J. Yang and N. Xiang, *Lab Chip*, 2020, **20**, 3485–3502.
86 K. Hood and M. Roper, *Phys. Rev. Fluids*, 2018, **3**, 094201.
87 X. Hu, J. Lin, D. Chen and X. Ku, *Microfluid. Nanofluid.*, 2020, **24**, 25.
88 C. Schaaf, F. Rühle and H. Stark, *Soft Matter*, 2019, **15**, 1988–1998.
89 S. Kahkeshani, H. Haddadi and D. D. Carlo, *J. Fluid Mech.*, 2016, **786**, R3.
90 C. Dietsche, B. R. Mutlu, J. F. Edd, P. Koumoutsakos and M. Toner, *Microfluid. Nanofluid.*, 2019, **23**, 83.
91 G. Segré and A. Silberberg, *J. Fluid Mech.*, 1962, **14**, 136–157.
92 J.-P. Matas, V. Glezer, É. Guazzelli and J. F. Morris, *Phys. Fluids*, 2004, **16**, 4192–4195.
93 J. F. Edd, D. Di Carlo, K. J. Humphry, S. Köster, D. Irimia, D. A. Weitz and M. Toner, *Lab Chip*, 2008, **8**, 1262–1264.
94 S. C. Hur, H. T. K. Tse and D. D. Carlo, *Lab Chip*, 2010, **10**, 274–280.
95 Y. Gao, P. Magaud, L. Baldas, C. Lafforgue, M. Abbas and S. Colin, *Microfluid. Nanofluid.*, 2017, **21**, 154.
96 Y. Gao, P. Magaud, C. Lafforgue, S. Colin and L. Baldas, *Microfluid. Nanofluid.*, 2019, **23**, 93.
97 X. Hu, J. Lin and X. Ku, *Phys. Fluids*, 2019, **31**, 073306.
98 A. Gupta, P. Magaud, C. Lafforgue and M. Abbas, *Phys. Rev. Fluids*, 2018, **3**, 114302.
99 G. D'Avino and P. L. Maffettone, *Microfluid. Nanofluid.*, 2019, **23**, 82.
100 F. Del Giudice, G. D'Avino, F. Greco, P. L. Maffettone and A. Q. Shen, *Phys. Rev. Appl.*, 2018, **10**, 064058.
101 L. Liu, H. Xu, H. Xiu, N. Xiang and Z. Ni, *Analyst*, 2020, **145**, 5128–5133.
102 A. M. Leshansky, A. Bransky, N. Korin and U. Dinnar, *Phys. Rev. Lett.*, 2007, **98**, 234501.
103 X. Lu, C. Liu, G. Hu and X. Xuan, *J. Colloid Interface Sci.*, 2017, **500**, 182–201.
104 M. Villone, G. D'avino, M. Hulsen, F. Greco and P. Maffettone, *J. Non-Newtonian Fluid Mech.*, 2013, **195**, 1–8.
105 F. Del Giudice, S. Sathish, G. D'Avino and A. Q. Shen, *Anal. Chem.*, 2017, **89**, 13146–13159.
106 G. D'Avino, M. A. Hulsen and P. L. Maffettone, *Comput. Fluids*, 2013, **86**, 45–55.
107 A. Jeyasountharan, K. Shahrivar, G. D'Avino and F. Del Giudice, *Anal. Chem.*, 2021, **93**, 5503–5512.
108 G. D'Avino and P. L. Maffettone, *Meccanica*, 2020, **55**, 317–330.
109 M. Asghari, X. Cao, B. Mateescu, D. van Leeuwen, M. K. Aslan, S. Stavrakis and A. J. deMello, *ACS Nano*, 2020, **14**, 422–433.
110 E. W. Kemna, R. M. Schoeman, F. Wolbers, I. Vermes, D. A. Weitz and A. Van Den Berg, *Lab Chip*, 2012, **12**, 2881–2887.
111 T. P. Lagus and J. F. Edd, *RSC Adv.*, 2013, **3**, 20512–20522.
112 R. Ramji, M. Wang, A. A. S. Bhagat, D. Tan Shao Weng, N. V. Thakor, C. Teck Lim and C.-H. Chen, *Biomicrofluidics*, 2014, **8**, 034104.
113 R. M. Schoeman, E. W. Kemna, F. Wolbers and A. van den Berg, *Electrophoresis*, 2014, **35**, 385–392.
114 X. Xu, F. Tian, X. Liu, R. M. Parker, Y. Lan, Y. Wu, Z. Yu, O. A. Scherman and C. Abell, *Chem. – Eur. J.*, 2015, **21**, 15516–15519.
115 S. Sajjadi, M. Alroaithi, A. S. Chaurasia and F. Jahanzad, *Langmuir*, 2019, **35**, 12731–12743.
116 V. A. Turek, Y. Francescato, P. Cadinu, C. R. Crick, L. Elliott, Y. Chen, V. Urland, A. P. Ivanov, L. Velleman and M. Hong, *et al.*, *ACS Photonics*, 2016, **3**, 35–42.

117 Y. Ding, P. D. Howes and A. J. deMello, *Anal. Chem.*, 2019, **92**, 132–149.

118 K. Matuła, F. Rivello and W. T. Huck, *Adv. Biosyst.*, 2020, **4**, 1900188.

119 A. Sattari, P. Hanafizadeh and M. Hoorfar, *Adv. Colloid Interface Sci.*, 2020, 102208.

120 K. Doufène, C. Tourné-Péteilh, P. Etienne and A. Aubert-Pouëssel, *Langmuir*, 2019, **35**, 12597–12612.

121 Y. Dou, B. Wang, M. Jin, Y. Yu, G. Zhou and L. Shui, *J. Micromech. Microeng.*, 2017, **27**, 113002.

122 F. Fontana, J. P. Martins, G. Torrieri and H. A. Santos, *Adv. Mater. Technol.*, 2019, **4**, 1800611.

123 L. Li, P. Wu, Z. Luo, L. Wang, W. Ding, T. Wu, J. Chen, J. He, Y. He and H. Wang, *et al.*, *ACS Sens.*, 2019, **4**, 1299–1305.

124 Y. Wang, T. Cao, J. Ko, Y. Shen, W. Zong, K. Sheng, W. Cao, S. Sun, L. Cai and Y.-L. Zhou, *et al.*, *Adv. Sci.*, 2020, **7**, 1903463.

125 E. Z. Macosko, A. Basu, R. Satija, J. Nemesh, K. Shekhar, M. Goldman, I. Tirosh, A. R. Bialas, N. Kamitaki and E. M. Martersteck, *et al.*, *Cell*, 2015, **161**, 1202–1214.

126 H.-S. Moon, K. Je, J.-W. Min, D. Park, K.-Y. Han, S.-H. Shin, W.-Y. Park, C. E. Yoo and S.-H. Kim, *Lab Chip*, 2018, **18**, 775–784.

127 Y. Ren, Z. Liu and H. C. Shum, *Lab Chip*, 2015, **15**, 121–134.

128 I. C. Clark and A. R. Abate, *Lab Chip*, 2018, **18**, 3598–3605.

129 A. R. Abate, C.-H. Chen, J. J. Agresti and D. A. Weitz, *Lab Chip*, 2009, **9**, 2628–2631.

130 G.-R. Yi, T. Thorsen, V. N. Manoharan, M.-J. Hwang, S.-J. Jeon, D. J. Pine, S. R. Quake and S.-M. Yang, *Adv. Mater.*, 2003, **15**, 1300–1304.

131 L. Lei, X. Tang, P. Zhu, Z. Kang, T. Kong and L. Wang, *J. Mater. Chem. B*, 2017, **5**, 6034–6041.

132 V. Gundabala, S. Martinez-Escobar, S. Marquez, M. Marquez and A. Fernandez-Nieves, *J. Phys. D: Appl. Phys.*, 2013, **46**, 114006.

133 J. Wang, H. Le-The, Z. Wang, H. Li, M. Jin, A. van den Berg, G. Zhou, L. I. Segerink, L. Shui and J. C. Eijkel, *ACS Nano*, 2019, **13**, 3638–3648.

134 S. Okushima, T. Nisisako, T. Torii and T. Higuchi, *Langmuir*, 2004, **20**, 9905–9908.

135 T. Nisisako, S. Okushima and T. Torii, *Soft Matter*, 2005, **1**, 23–27.

136 N. Wang, C. Semprebon, H. Liu, C. Zhang and H. Kusumaatmaja, *J. Fluid Mech.*, 2020, **895**, A22.

137 A. Tiribocchi, A. Montessori, M. Lauricella, F. Bonaccorso, S. Succi, S. Aime, M. Milani and D. Weitz, *Nat. Commun.*, 2021, **12**, 82.

138 A. C. H. Tsang, M. J. Shelley and E. Kanso, *Soft Matter*, 2018, **14**, 945–950.

139 G. Mishler, A. C. H. Tsang and O. S. Pak, *J. Nonlinear Sci.*, 2018, **28**, 1379–1396.

140 A. Dhar, P. Burada and G. R. Sekhar, *Phys. Fluids*, 2020, **32**, 102005.

141 A. Isozaki, J. Harmon, Y. Zhou, S. Li, Y. Nakagawa, M. Hayashi, H. Mikami, C. Lei and K. Goda, *Lab Chip*, 2020, **20**, 3074–3090.

142 N. Nitta, T. Sugimura, A. Isozaki, H. Mikami, K. Hiraki, S. Sakuma, T. Iino, F. Arai, T. Endo and Y. Fujiwaki, *et al.*, *Cell*, 2018, **175**, 266–276.

143 A. Isozaki, H. Mikami, H. Tezuka, H. Matsumura, K. Huang, M. Akamine, K. Hiramatsu, T. Iino, T. Ito and H. Karakawa, *et al.*, *Lab Chip*, 2020, **20**, 2263–2273.